Novel X-Ray Imaging Techniques for *Ex-Situ* and *Operando* Study of Polymer Electrolyte Fuel Cells

Submitted By
STANLEY J. NORMILE

IN PARTIAL FULFILLMENT OF THE REQUIREMENTS FOR THE DEGREE OF

MASTERS OF SCIENCE IN MECHANICAL ENGINEERING

School of Engineering
Tufts University
Medford, Massachusetts

May 2018

Signature of Author:
Stanley J. Normile

Certified By:
Professor Iryna V. Zenyuk
Department of Mechanical Engineering
Department of Chemical and Biological Engineering
Tufts University

Committee:
Professor Marc Hodes
Department of Mechanical Engineering
Tufts University

Committee:
Professor Matthew Panzer
Department of Chemical and Biological Engineering
Tufts University

Abstract

Polymer electrolyte fuel cells are a promising clean alternative to conventional internal combustion engines for transportation applications. Among the issues preventing full-scale commercialization are the high cost of platinum (Pt), transport losses associated with ionomer distribution in the catalyst layer, and management of the water which is produced as a by-product of the fuel cell reaction. The morphology of the catalyst layer plays an important role in the aforementioned challenges. X-ray computed tomography (CT) is an ideal way to study this morphology as it is non-destructive and can resolve structures on both the micro- and nano-scales. Presented here is a novel way to image Pt and ionomer in catalyst layers using cesium staining and x-ray absorption near edge spectroscopy (XANES). Additionally, this work focuses on overcoming barriers in operando hardware design for synchrotron x-ray imaging, focusing on both micro- and nano-scales, which will help explain the interplay between morphology and transport processes, as well as water management. The fuel cells presented here show significant promise, as they can combine the study of electrochemical performance with that of water distribution in fuel cell components during operation.

Acknowledgements

I would first and foremost like to thank my advisor, Professor Iryna Zenyuk for mentoring me for the past three years. Professor Zenyuk inspired me to conduct my research at the highest possible level. Without her guidance and encouragement I know that I would not have been able achieve half of what I did in the past two years.

I would also like to thank my lab mates who contributed to this work: Dinesh Sabarirajan, our fearless lab manager, whose electrochemical expertise was indispensable. Andrew Shum was always ready to help with reconstructions. He also worked tirelessly to take the best possible images with the micro CT sample holder that I designed. Jiangjin Liu and Emily Leonard were the best desk neighbors I could ask for. Osvaldo Calzada kept me company through long and stressful beamtimes. Liam Connolly led the design of the original nano CT cell upon which my later designs were based.

I would like to thank Professors Chris Rogers, William Messner, and Pratap Misra for mentoring me in my teaching assistantships. I truly enjoyed working with each of you.

I would like to also thank my friends and family who encouraged and supported me for the past two years.

Finally, I would like to thank my funding sources: The United States Department of Energy, the National Science Foundation, and the Mechanical Engineering Department at Tufts University.

Table of Contents

1 Introduction 1
1.1 Need for characterization 1
1.2 Imaging Techniques 4
1.2.1 Neutron Imaging 6
1.2.2 Micro CT 7
1.2.3 Beamlines 13
1.3 Morphological properties 14
1.3.1 Measuring Porosity and Tortuosity 16
2 Tomography Theory 18
2.1 Chapter Introduction 18
2.2 Optics Theory 19
2.2.1 Free Space Wave Equation 19
2.2.2 Refraction 20
2.2.3 Absorption 21
2.2.4 Intensity 22
2.2.5 Interference 24
2.3 Application to X-ray Tomography 25
2.4 Guide to use theory for experiment design to predict effectiveness of phase vs absorption-contrast imaging 27
2.5 XANES Imaging 30
2.6 Chapter Conclusion 32
3 Platinum Loading and Distribution 32
3.1 Chapter Introduction 32
3.1.1 Nano-Structured Thin-Film Electrodes 33
3.1.2 Ionomer Distribution 35
3.2 Sample Procedure 37
3.3 Image Processing 37
3.4 Results 41
3.4.1 Pt distribution 41
3.4.2 Porous matrix 42
3.5 Chapter Conclusion 44
4 Two Energy XANES Imaging 44
4.1 Chapter Introduction – Imaging problems with Cs staining 44
4.2 Sample Preparation 45
4.3 Imaging procedure 46
4.3.1 Image processing procedure 47
4.4 Results/Discussion 48
4.4.1 Image processing discussion 48
4.4.2 Separating Pt from Cs 48
4.4.3 Importance of separating Pt from Cs 49
4.4.4 Finding for this material in particular 52
4.5 Chapter Conclusion 55
5 Micro CT *Operando* 55
5.1 Chapter Introduction 55

5.2 Design 56
5.2.1 Material selection 56
5.2.2 Flow channels 61
5.2.3 Electrical and Thermal 64
5.3 Discussion/Results 67
5.4 Chapter Conclusion 70
6 Nano CT *Operando* 70
6.1 Chapter Introduction 70
6.2 Design 70
6.2.1 Material selection 70
6.2.2 Cell Geometry 72
6.3 Issues with First Generation Nano CT Cell 76
6.3.1 MEA Movement 76
6.3.2 Electrical Conductivity 77
6.3.3 Mechanical Compression 77
6.3.4 Beam Damage and Reconstructions 78
6.4 Second Generation Cell – SSRL 79
6.4.1 Results 81
6.5 Third Generation Cell – ESRF 85
6.6 Fourth Generation Cell – Under Development 88
6.7 Chapter Conclusion 89
7 Conclusions and Future Work 90
7.1 Conclusion 90
7.2 Future Work 93

Table of Figures

Figure 1-1 Polarization curve of a PEM fuel cell 1
Figure 1-2 a) Nano CT image of 3M CCM (highly attenuating features bright) b) diagram of cathode catalyst layer with transport paths highlighted [2] c) TEM image of platinum sites of cathode catalyst layer (highly attenuating features dark) 3
Figure 1-3 Resolution and field of view of various imaging techniques: FIB-SEM (purple), Nano CT (yellow), Micro CT (red), Neutron imaging (blue) 5
Figure 1-4 Cell alignments a) horizontal b) vertical [8] 7
Figure 1-5 Operando cell developed by Eller et al. [8] 8
Figure 1-6 Water separation in GDL using image subtraction a) dry GDL b) wet GDL c) differential image (water) [8] 9
Figure 1-7 Operando cell designed by White et al. [9] 11
Figure 1-8 Beam damage to operando cell [8] 13
Figure 1-9 Comparison of geometric (Fast Marching Method, Pore Centroid Method), Flux-based simulation (TauFactor, Heat Flux Simulation), and Experimental (Diffusion Cell) Tortuosity for four different samples [20] 18
Figure 2-1. Zernike phase contrast imaging a) diagram of phase ring placement [30] b) absorption contrast imaging c) phase contrast imaging (ideal) d) phase contrast imaging (real) [31] 26
Figure 2-2. Various optical properties of Platinum (Blue), Cesium (Red), Carbon (Green), and Nafion Ionomer (black) as a function of photon energy. a) Refractive index decrement (δ) b) absorption index (β) c) attenuation coefficient (μ) d) mass attenuation coefficient (μ/ρ) 29
Figure 2-3. a) Ni (blue) and Cu (red) attenuation coefficients b) optical depth as a function of photon energy for a NiCu sample about Ni edge 31
Figure 3-1 Histogram of the image in Figure 3-2c 38
Figure 3-2. Thresholding procedure a) phase contrast image b) thresholded phase contrast image (solid phase white) c) absorption contrast image d) thresholded absorption contrast image (platinum white) e) thresholded absorption contrast image (ionomer white) f) absorption contrast image with ionomer highlighted 39
Figure 3-3. Volume renderings of the thresholded images in Figure 3-2 a) all solid phase b) ionomer c) platinum d) ionomer and platinum e) carbon, ionomer and Pt 40
Figure 3-4. Platinum distribution a-c) medium surface area carbon d-f) high surface area carbon a,d) Pt volume fraction vs Wh/C b,e) average Pt agglomerate radius c,f) Pt agglomerate size distribution 41
Figure 3-5. Otsu radius effects a) average pore size b) average solid size c) porosity d) pore size distribution and e) solid size distribution for Otsu radius of 60 pixels 42
Figure 3-6. Properties of catalysts as a function of Wh/C a) tortuosity factor b) porosity. 2054 refers to high surface area carbon, 2033 refers to medium surface area carbon, IP refers to in plane, and TP refers to thru plane 43
Figure 4-1. Scans were performed at 11.5 and 11.7 keV to take advantage of the Platinum L3 absorption edge 47
Figure 4-2. a) 11.7 keV image b) 11.5 keV image c) result of subtracting (b) from (a) d-f) thresholded images of respective scans. The bright spot in (a) could be either Pt or Cs. By subtracting (b) which Cs only, (c) shows Pt only. 50

Figure 4-3. Volume renderings of a) Platinum b) Ionomer c) Platinum and Ionomer. d) Cross-section image with Pt (green) and Ionomer (blue) highlighted 53
Figure 4-4. a) Ni (blue) and Cu (red) attenuation coefficients b) optical depth as a function of photon energy for a NiCu sample c) radiographs at various energies 54
Figure 5-1. Attenuation of ¼ inch (0.635 cm) plates of Aluminum (blue), Graphite (red), and PEEK with 300 nm of sputtered Gold (green) as a function of photon energy over a typical micro CT range 57
Figure 5-2. Simple supports uniform load 59
Figure 5-3. Micro CT Operando Cell 60
Figure 5-4. Compression pattern of Cell a) previous designs b) final design 61
Figure 5-5. Fuel Cell and Electrolyzer flow channel designs. Marked dimensions are in millimeters and all channels are 1mm wide X 1mm deep with 1mm land. A) Fuel Cell serpentine channel design b) electrolyzer parallel channel design c) photo of electrolyzer design. The white alignment pins at the top and bottom of the channel ensures that the anode and cathode channels are in precise alignment. The Copper electrical contact point reduces contact resistance between the plate and the wire 62
Figure 5-6. Micro CT cell images a) without alignment pins b) with alignment pins 63
Figure 5-7. Step response of Anode heater (blue) and Cathode heater (red) 65
Figure 5-8. a) Model for thermal analysis – the channel face is modeled as adiabatic, all other faces are modeled as having a convective heat transfer coefficient of 7.3 $Wm^{-2}K^{-1}$ b) Temperature distribution along graphite plate c) Temperature distribution along the length of the channel when the heater is set to 60 °C (blue) and 63 °C (red) 66
Figure 5-9. Micro CT operando images of a PGM-free fuel cell a) dry image b) wet image c) wet image with water highlighted d) water only e-h) through plane versions of (a-d) 68
Figure 6-1. Attenuation of ¼ inch Graphite plate (red), ¼ inch PEEK plate (green), 15 μm Kapton window (blue) over a typical nano CT range 71
Figure 6-2. Top view of nano CT cell where θ is the angle of the cell relative to the beam. The cell structure blocks x-rays from reaching the collector when $\theta < 16°$ 72
Figure 6-3. Flow Chamber – Blue arrows indicate gas supply, Red arrows indicate gas return 73
Figure 6-4. Nano CT cell base a) cutaway view with flow channels highlighted b) photo 74
Figure 6-5. Exploded view of the assembled nano CT operando cell 75
Figure 6-6. Mosaic of nano CT images a) without window in GDL b) with window in GDL 75
Figure 6-7. a) Flow chamber with added stability bars b) compression pattern 76
Figure 6-8. Beam damage to CCM a) sonogram and reconstructed tomogram of first scan after 20 minutes of beam exposure b) third scan after 60 minutes c) photo of MEA after scanning d) graph of CCM thinning due to beam damage 79
Figure 6-9. a) Radiographs of the nano CT cell CCM under progressively higher current conditions b) Current vs time curve for the 0.5, 0.3, and 0.1 V runs c) Percent increase in greyscale value (proportional to decrease in attenuation) of each image relative to the dry air image 81

Figure 6-10. a) Radiographs of the nano CT cell GDL under progressively higher current conditions b) Current vs time curve for the 0.7, 0.5, and 0.1 V runs c) Swelling of the GDL as tracked by measuring the distance between the gold fiducials marked in (a) 85
Figure 6-11. Nano CT cell graphite plate 86
Figure 6-12. Operando cell at ESRF a) micro CT mode b) 100 nm c) 50 nm 87
Figure 6-13. Generation IV nano CT cell a) flow chamber cell b) half-graphite cell c) exploded view of flow chamber cell 89

Table of Tables

Table 1-1 Imaging Techniques 5
Table 1-2 Micro CT Beamlines 13
Table 3-1. Linear Attenuation Coefficients of Catalyst Components..... 36
Table 3-2. Imaging Goals 36
Table 4-1. Properties of scans at the two energies. The combined Pt and Cs scan yields a significantly higher volume fraction and lower tortuosity than does the Cs only scan. The reported tortuosity is averaged across the three coordinate directions. 51
Table 5-1. Parameters for material selection 57
Table 6-1. Attenuation coefficients of CCM substances at 8 keV..... 83
Table 6-2. Attenuation of materials at 8 keV and 17.5 keV 86
Table 6-3. Nano CT cell design analysis 88

1 Introduction

1.1.1 Need for characterization

Fuel cells are electrochemical energy conversion devices that use hydrogen as fuel on the anode. The thermodynamic potential for the cell operating on hydrogen and oxygen is 1.23 V for standard conditions. As the current is drawn from the cell various losses occur that can be also called overpotentials, and consist of: activation, Ohmic and mass-transport or polarization losses. Fuel cells exhibit significant mass transport losses at high current densities, which severely limits their performance (Figure 1-1) [1].

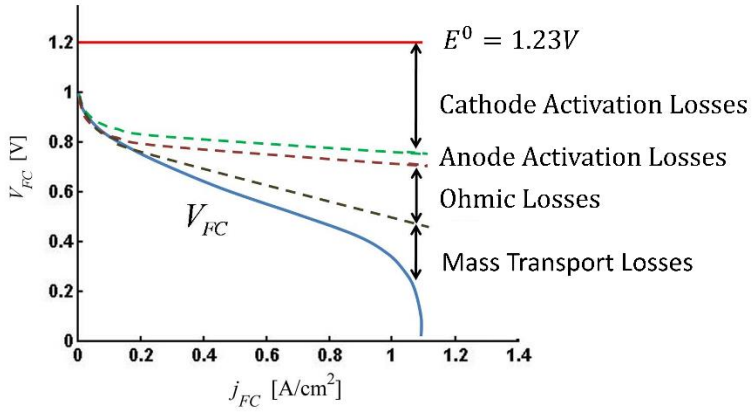

Figure 1-1 Polarization curve of a PEM fuel cell

Decreasing mass transport resistance is central to the design of new fuel cell components. Catalyst coated membranes (CCMs) consist of a membrane—either a proton exchange membrane (PEM) in the case of PEM fuel cells, or an anion exchange membrane (AEM) in the case of alkaline fuel cells—coated on both sides with a catalyst. This catalyst consists of a support material (usually carbon) with platinum (Pt) catalyst sites held together by an ionomer binder, such as Nafion® by DuPont. The catalyst is prepared as an ink, which is then sprayed onto the membrane. Alternatively, the catalyst can be

sprayed onto the gas diffusion layer (GDL) forming a gas diffusion electrode (GDE). The cathode catalyst layer is where the proton that has traversed the membrane recombines with the electron that traversed the external circuit and the oxygen to form water (1.1).

$$O_2 + 4H^+ + 4e^- \rightarrow 2H_2O \qquad (1.1)$$

The transport paths through the cathode catalyst layer are highlighted in Figure 1-2b. The ionomer serves the dual function of adhering the carbon support particles and serving as the proton conductor. The Pt serves as the electrocatalyst for the reaction (1.1), with two important caveats. The first is that the reaction is only takes place on the surface of the Pt, and the second is that all the species that participate in ORR need to reach Pt electrocatalyst for the reaction to happen. Due to its high cost, Pt should be used as sparingly as possible by maximizing its surface area to volume ratio. This can be accomplished most simply by reducing the loading of Pt and ensuring that the electrocatalyst is well-dispersed, as shown in Figure 1-2c. The TEM in Figure 1-2c shows 3 nm Pt particles dispersed onto the carbon support.

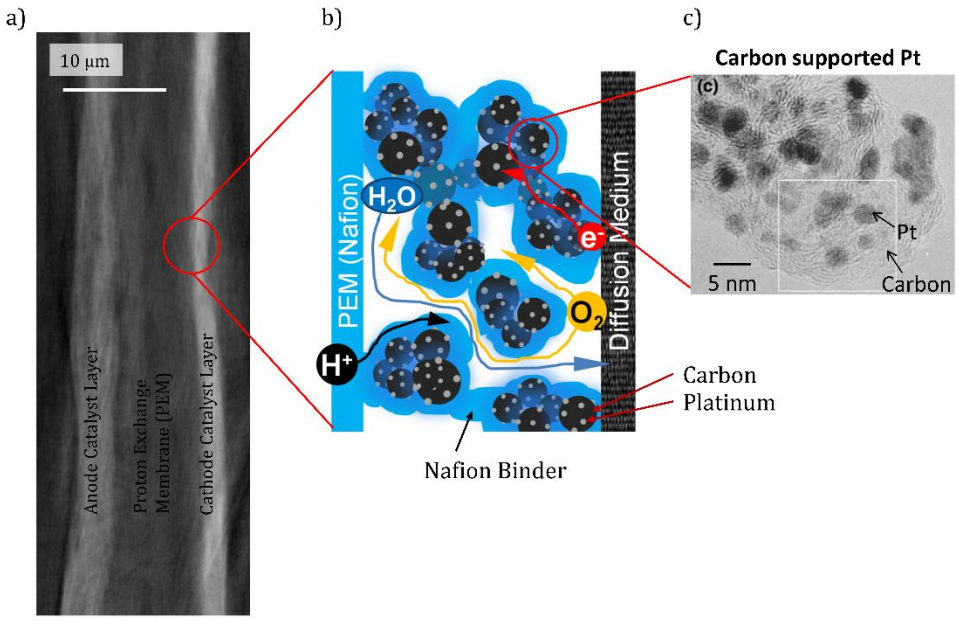

Figure 1-2 a) Nano CT image of 3M CCM (highly attenuating features bright) b) diagram of cathode catalyst layer with transport paths highlighted [2] c) TEM image of platinum sites of cathode catalyst layer (highly attenuating features dark)

There are three separate transport paths in the cathode catalyst layer: that of the proton through the ionomer, the oxygen and water through the pores, and the electron through the carbon. Understanding how the morphology of the catalyst layer affects transport processes is critical. This requires non-intrusive imaging techniques that can be combined with actual fuel cell operation to elucidate transport and water distribution under varied applied current densities. This work addresses three main questions: 1) the appropriate x-ray tools to study ionomer, carbon, electrocatalyst and water distributions. 2) The design of fuel cells that are x-ray transparent for the purpose of this study. 3) How to advance imaging techniques to capture both morphology and chemical information.

Before answering those main questions, it must be noted that the porous media tools that are available in petroleum community are not necessarily applicable here, where the media is thin. Thus, this work revisits some of the morphological properties from porous

media to reassess their applicability in the fuel cell field. The remaining of the introduction focuses on: 1) state-of-the-art imaging techniques and 2) porous media morphological parameters.

1.2 *Imaging Techniques*

There are two classes of imaging techniques used in this study. The first is *ex-situ* study, which refers to the imaging of components, such as CCMs and GDLs, outside of the fuel cell. This is typically done by cutting a small portion of material and mounting it on a pin for scanning. *Ex-situ* study is best suited for evaluating static properties, such as Pt and ionomer distributions, and porous matrix properties such as the porosity and tortuosity. The other class of techniques is *operando*, which refers to imaging fuel cell components inside the cell while the cell is running. *Operando* imaging is best for studying dynamic effects, such as water production and distribution. A third class of imaging, *in-situ*, is similar to *operando*, except the fuel cell is not running during scanning. This work focuses on *ex-situ* and *operando* imaging.

The need for morphological quantization described above exist on a continuum of length scales. Figure 1-3 shows the field of view and resolution of various imaging techniques that can be used to study fuel cell components.

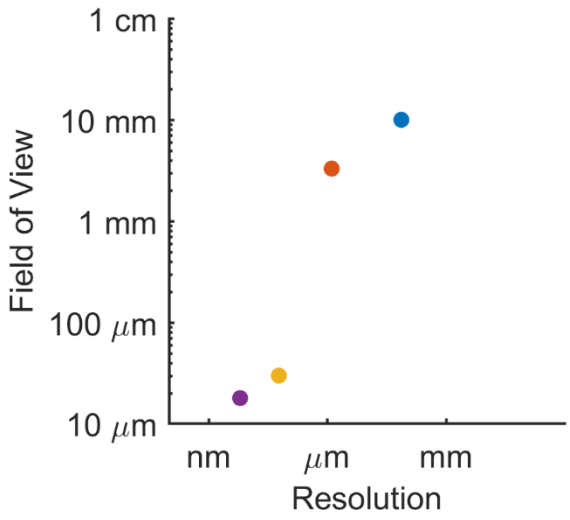

Figure 1-3 Resolution and field of view of various imaging techniques: FIB-SEM (purple), Nano CT (yellow), Micro CT (red), Neutron imaging (blue)

While electron techniques such as SEM, TEM, and FIB-SEM have exceptional resolutions, none of them are suitable for this study. Although 3D imaging is possible with the TEM, it can only image thin samples, on the order of 100 nm [3], and SEM is a 2D technique. This makes them both unable to visualize thick components in 3D, which is necessary to accurately describe their morphology. FIB-SEM, while able to resolve images in 3D, is a destructive technique. Additionally, none of the electron techniques can image through any type of sample holder for *operando* study. That leaves x-ray CT and neutron imaging, both of which have been used previously for *ex-situ* and *operando* study. While neutron imaging is limited to 2D, it has the advantage of being able to image through metal sample holders, making it practical for *operando* study. Table 1-1 summarizes the available techniques.

Table 1-1 Imaging Techniques

Technique	FOV	Resolution	3D	Destructive	Image through sample holder
Neutron	10 mm	75 µm	No	No	Yes – all kinds

Micro CT	3.3 mm	1.3 µm	Yes	No	Yes – most non-metal holders
Nano CT	30 µm	60 nm	Yes	No	Depends on energy – non-metal holders only
FIB-SEM	18 µm	6.3 nm	Yes	Yes	No

The resolution and field of view (FOV) of micro CT are in an ideal range to study the gas diffusion layer (GDL), the interface between the CCM and the GDL, and the channels of the fuel cell. Nano CT, on the other hand, is better for studying the CCM and the catalyst layers. Nano CT can be used to quantify the platinum distribution, ionomer distribution, and porous structure of the catalyst layer. For the *ex-situ* study of catalyst layers, the easiest way to study the catalyst is to spray it onto a Kapton® or Mylar® liner, rather than the membrane. Liners are sturdier than membranes and, unlike membranes, cannot be damaged by x-rays. This electrode on liner can then be imaged using nano CT. Prior work in *operando* imaging has used neutron and micro CT exclusively, and is summarized here.

1.2.1 Neutron Imaging

The dynamic nature of the water production means that the water distribution in the porous matrices is best studied using *operando* techniques. This poses a unique set of challenges as the material of the fuel cell itself must be transparent to the imaging method being used. Coz et al. and Seweryn et al. used neutron imaging to study a planar air breathing fuel cells and PEM electrolyzers respectively since neutrons can be used to image through metals [4, 5]. This simplified their hardware design as they could simply use conventional fuel cells. Additionally, the water cross-section for neutrons is large,

making it close to a perfect method for probing water. The disadvantage of this technique is that the resolution is only 75 µm, which is not fine enough to see the distribution water in the catalyst layer (~10 µm) and within the pores of the GDL (~30 µm). The other disadvantage is that the neutron flux is lower than x-ray fluxes, making tomography experiments impossible, hence only radiography experiments are currently performed.

1.2.2 Micro CT

In order to visualize the water distribution in the pores of components, such as GDLs, 3D tomographic study is necessary. Manke et al. developed the first fuel cell for x-ray study by drilling an 8 mm hole in the metallic plate of a fuel cell and imaging through it using x-ray radiography [6]. This offered a significant improvement in resolution over neutron imaging (1.5 µm vs 75 µm), however the field of view was limited to 7mm. Schneider et al. built upon these results and developed the first cell capable of being imaged with tomography [7]. Schneider's cell is oriented so that the membrane electrode assembly (MEA) is horizontal with respect to the plane of the beam, as shown in Figure 1-4a. This has the advantage of ensuring that the entire MEA/GDL area is within the field of view.

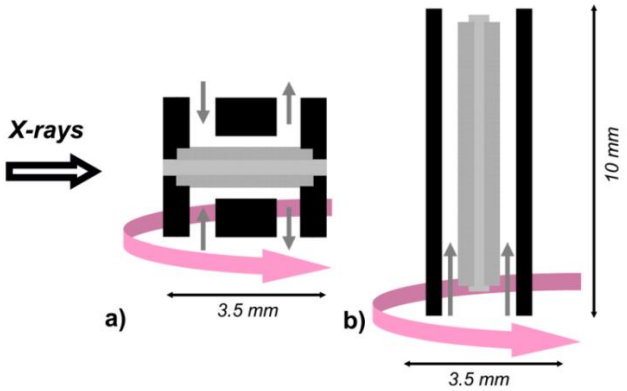

Figure 1-4 Cell alignments a) horizontal b) vertical [8]

Eller et al. designed a horizontal cell based on that of Schneider, but noted that the flow channels were too short for the velocity profile to fully develop [8]. This meant that the flow in those channels could not be assumed to be representative of that in a full-sized fuel cell. To counter this, they designed a vertically oriented cell (also known as a standing cell, Figure 1-4b), which has a channel length of 12.4 mm and an active area of 30.5 mm^2 shown in Figure 1-5.

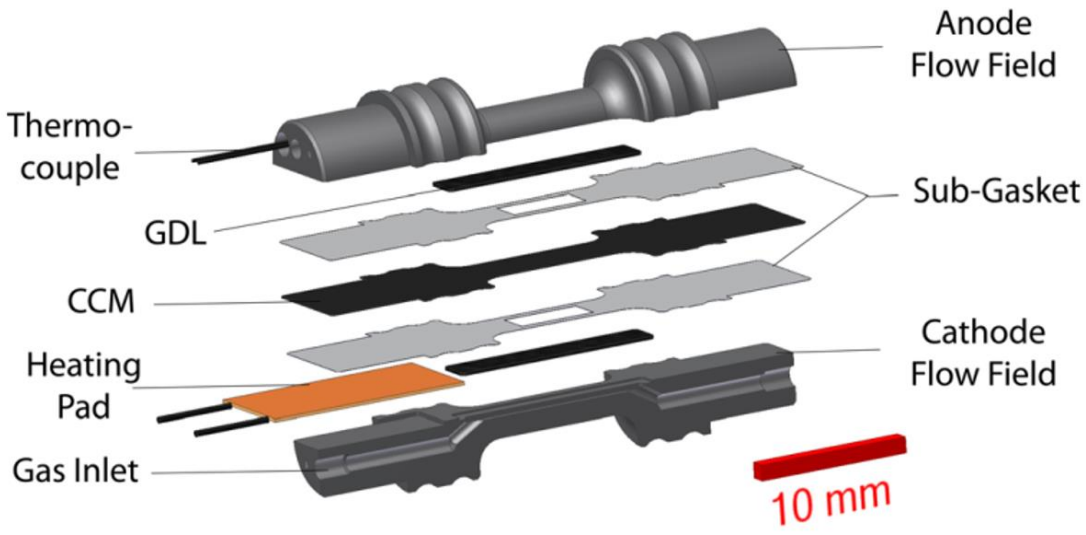

Figure 1-5 Operando cell developed by Eller et al. [8]

Unlike the horizontally oriented cell, the vertically oriented cell's active area is too large to be imaged all at once, since the beam height at the TOMCAT beamline of the Swiss Light Source at Paul Scherrer Institute in Switzerland is only 5.1mm. This can be countered by taking several scans and stitching the images together into a composite image called a mosaic.

The cell was made from a carbon composite (BMA5, SGL Technologies). This composite is graphite based and has good electrical and thermal conductivity. While not

explicitly stated, these plates are likely used at the current collectors of the cell, due to their high conductivity. The channel is 0.8 mm wide and 0.3 mm deep. Compression is provided by small O-rings around the recesses in the thick portion. The cell was able to maintain current densities up to 1 A/cm^2 [8]. This cell was the inspiration for the cell presented in Chapter 5.

Eller et al. also pioneered a way to segment the water in the GDL in the resultant image. The cell was run for some time, in order to establish steady state operating conditions. It was then scanned (this image is known as the "wet" image), after which dry gases were passed at elevated temperatures in order to dry out the GDL. The cell was then scanned again (this is known as the "dry" image). The dry and wet images were aligned, then the dry image was subtracted from the wet image to form an image that consists exclusively of water, as shown in Figure 1-6 [8].

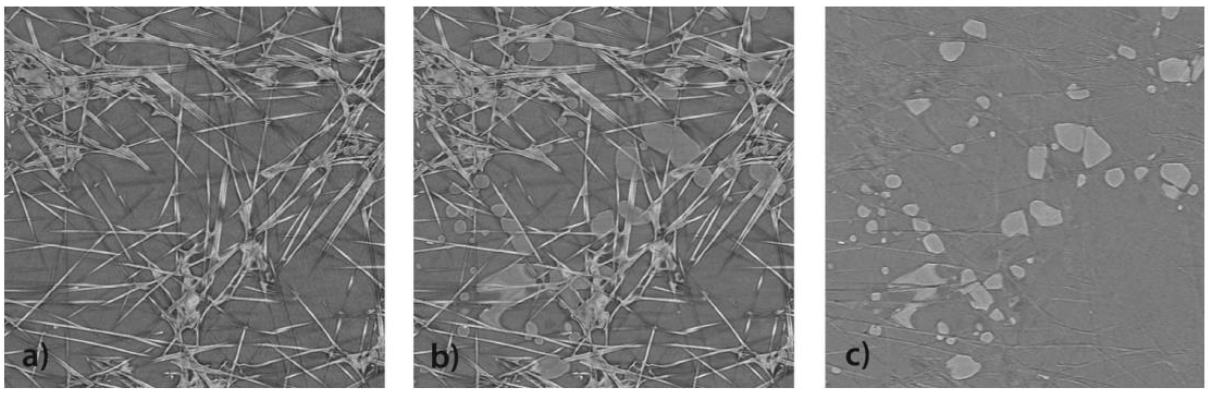

Figure 1-6 Water separation in GDL using image subtraction a) dry GDL b) wet GDL c) differential image (water) [8]

If implemented in *operando* study, this procedure runs the risk of over drying the membrane, causing it to shrink and making the images impossible to align. The morphology of the GDLs is not sensitive to RH but membrane swelling can be harmful

for image alignment due to swelling under higher RH. In order to ensure this problem is avoided, the procedure in presented in Chapter 5 for operando cell takes the dry image with 100% RH air flowing in the cell, as opposed to dry air. Excess water is avoided by taking the OCV image before the cell is run for the wet image.

White et al. developed an operando cell for a lab-scale x-ray CT machine which featured a 3D printed holder [9]. They were the first to use the Beer-Lambert law to predict the attenuation of their sample holder, in order to ensure that it was transparent enough. The use of 3D printing offers the advantage of being able to rapidly change the flow field design. This allows for the study of the effect of the flow field pattern on the fuel cell performance, which was not previously available. The Stratasys Objet RGD525 high temperature material that the cell was made from has low x-ray absorbance compared to that of graphite, however it is not electrically conductive. They solved this by using a copper current collector as shown in Figure 1-7. The fact that the current collector is only in contact with a small portion of the active area severely reduced the electrochemical performance of the cell. White et al. were only able to record a current density of 0.1 A/cm^2 [9], a full order of magnitude smaller than that of Eller et al.

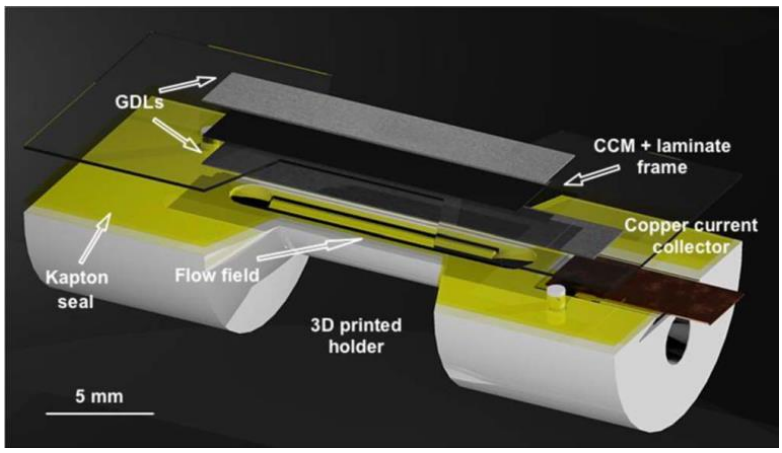

Figure 1-7 Operando cell designed by White et al. [9]

White et al. observed that the CCM swelled from 20 to 25 µm when the cell was run, due to ionomer hydration [9]. They were limited by their 1.8 µm resolution, which is not high enough to visualize any features within the CCM. This highlights the need for *operando* nano CT study.

One problem many authors faced was beam damage to the MEA/GDL [7-9]. Some experiments show strong correlation between the x-ray exposure and the degradation of performance, while others do not. The radiation dose absorbed by an object under the influence of x-rays is given by equation (1.2) [10].

$$R = \frac{NTE\mu}{\rho} \tag{1.2}$$

Where R is the radiation dose in keV/g (often converted to rad), N is the flux density in photons/cm^2/s, T is the exposure time in s, E is the photon energy in keV, μ is the linear attenuation coefficient in cm^{-1}, and ρ is the density in g/cm^3. It should be noted that the attenuation coefficient is inversely proportional to photon energy, so a smaller fraction of incident photons are absorbed at high energies. Lim et al. studied beam damage to the

carbon-binder matrix of a Li-ion electrode and found minimizing the radiation damage is best accomplished with a combination of limiting the accumulated x-ray dose and using an intermittent exposure [11]. Vaselabadi et al. suggest that radiation damage to polymers has an onset dose, below which little damage can be seen [12]. Lim et al. tested this by scanning their sample with each exposure radiation dose less than the hypothesized onset dose for their material and a 3-8s pause between each exposure. This method showed a significant reduction in beam damage [11], however poses a problem for *operando* study. Water droplets will only appear clearly if they are present for the entire scan duration [8]. If a droplet is removed half way through a scan, it will be present in some tomograms, and not in others, blurring the phase boundary in the reconstructed image. Pausing between exposures to minimize beam damage will increase the scan time and make it more likely that a droplet move between exposures.

While Lim et al. measured beam damage visually, Eller et al. measured it by tracking the voltage of their *operando* cell (while maintaining a constant current density) during irradiation. They found that the vertically oriented cell exhibited significantly more damage than the horizontally oriented cell [8, 13]. They also found that once the cell started losing voltage after being irradiated, the losses continued even after the beam was shut off, as seen in Figure 1-8.

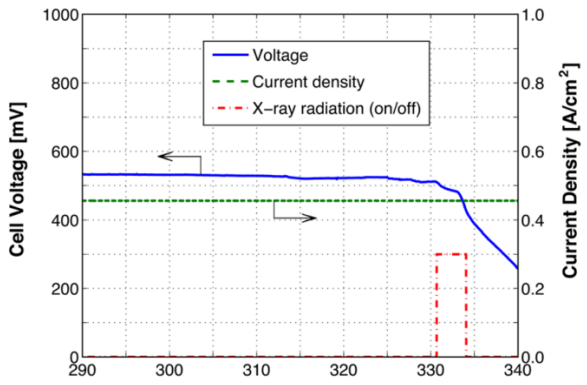

Figure 1-8 Beam damage to operando cell [8]

Eller et al. noted a high concentration of water droplets near the cathode catalyst layer. They also noticed a high concentration of water under the land, but noted that since their cell only had one channel, this did not account for realistic edge effects [8]. They also noted in their later work that the absorbed energy from the beam influences water production and removal [13]. White et al. noticed significant water pooling at the edges of the channels adjacent to the cathode GDL-land interface, due to the low fluid velocity at that point [9]. White's cell was operated at room temperature (as opposed to Eller's at 40°C), so evaporation is not expected to play any part in the water removal [14].

1.2.3 Beamlines

Several synchrotrons have micro CT beamlines, among them are 8.3.2 at the Advanced Light Source (ALS) at Berkley National Lab in Berkley, CA; 2-BM at the Advanced Photon Source (APS) at Argonne National Lab in Lemont, IL; and TOMCAT at the Swiss Light Source at Paul Scherrer Institute (PSI) in Villigen, Switzerland. Table 1-2 provides an overview of the capabilities of these beamlines.

Table 1-2 Micro CT Beamlines

	8.3.2 at ALS	2-BM at APS	TOMCAT at PSI

Energy Range	6-43 keV	11-35 keV	8-45 keV
Resolution Range	0.9-9 μm	1.3 μm	3 μm
Field of View Range	3.6-36 mm	3.3 mm	5.6 mm
Imaging Techniques	Absorption, Phase Contrast	Absorption, Phase Contrast	Absorption, Phase Contrast
High-speed tomography	Not possible	Under development	Yes

One promising imaging technique is high speed tomography, which has already been used in the battery community to study thermal runaway, as it can image with an exposure time of 0.35 ms as opposed to the usual 1s [15]. If this technique were applied to *operando* fuel cell study, it would virtually eliminate the risk of a water droplet moving during the scan. So far, the practical limitations of rotating the cell quickly enough (75 rpm) have prevented this technique from being used extensively. Xu et al. [16] used sub-second imaging to diagnose the signal-to-noise ratio in fuel cell channel with droplets of water of various sizes. The main challenge of the technique is the fast rotation, which is not limited by the air-bearing stages that most of the beamlines have but rather limited by all the tubing and wiring that go into the cell. Rotary unions and slip rings are needed to enable cell rotation with the adjoining components.

1.3 *Morphological properties*

The transport of species through porous media is highly dependent on the material structure. This structure can be quantified with parameters such as the porosity, pore size

distribution, and tortuosity. The porosity and pore size distribution represent the volume fraction and distribution of sizes of the phase of the media through which the species will diffuse. In the case of water and oxygen diffusing through the catalyst layer, they refer to the void space, but when describing the proton transport, they refer to the ionomer. Tortuosity is more difficult to define, as the literature does not agree on its definition and what it encompasses [17]. The most basic definition of tortuosity is the ratio of the length of a molecule's path through a porous media to the Euclidian distance between the inlet and exit of that path (1.3).

$$\tau = \frac{L_e}{L} \tag{1.3}$$

Where τ is the tortuosity, L_e is the effective length travelled by the diffusing species, and L is the Euclidean distance between the inlet and exit. The tortuosity factor (1.4) is equal to the square of the tortuosity, however it accounts for more than just geometric effects.

$$\kappa = \tau^2 = \left(\frac{L_e}{L}\right)^2 \tag{1.4}$$

Where κ is the tortuosity factor. The most common use of the tortuosity factor is in the equation for the effective diffusivity of species A through a porous media (1.5).

$$\left(D_A\right)_{eff} = \frac{\varepsilon}{\kappa} D_A \tag{1.5}$$

Where D_A is the diffusivity of species A, $(D_A)_{eff}$ is the effective diffusivity, and ε is the porosity [18, 19]. A detailed derivation of this equation may be found in Epstein's famous paper [18]. This equation has the downside of bundling all retarding factors that

are not porosity into one term, the tortuosity factor. This definition accounts for not only the tortuous path that a diffusing species must take, but constriction due to varying pore sizes, as well as dead ends in pore channels.

1.3.1 Measuring Porosity and Tortuosity

The most common method to experimentally measure tortuosity in the fuel cell community is to measure the effective diffusivity $(D_A)_{eff}$ and compare it to the bulk diffusivity using (1.5). This is done by measuring the gas composition at the inlet and exit of the porous structure [20, 21]. Filling a porous media with electrically conductive liquid and measuring the specific conductivity between the inlet and exit of the porous structure is a common measurement technique, however it is not possible on porous carbon electrodes since the carbon itself is conductive. Additionally, these conductivity measurements do not always produce results that are consistent with either the theory or other experimental methods [22].

In addition to measuring tortuosity experimentally, it can be measured using imaging. One method of probing the conductivity is nuclear magnetic resonance spectroscopy [23], which has shown similar results to that of electrical conductivity measurements for long observation times [22]. The tortuosity can also be measured using x-ray computed tomography (CT). Once the sample has been imaged and thresholded, the resulting 3D volume can be analyzed. The porosity is easy to find, as it is simply the volume fraction of the void phase. There are two basic approaches to computing the flow channels and therefore the tortuosity. The first is a purely geometric approach in which the algorithm finds the shortest path through the porous media between two points and compares it to

the minimum Euclidean distance between those two points to find the tortuosity. The second approach is to simulate the flux between two points and back calculate the tortuosity factor from (1.5). It should be noted that the first method finds the tortuosity and the second method finds the tortuosity factor. Tjaden et al. noted that, even when the tortuosity factor is square rooted to find the tortuosity, the flux-based algorithms provide consistently higher tortuosity than the purely geometric algorithms. This is a result of the fact that the flux-based algorithms take into account constriction due to variation in pore diameters, whereas the purely geometric algorithms do not [20].

One of the flux-based algorithms is TauFactor, an open source third party Matlab application. TauFactor applies a concentration gradient to the matrix and iteratively calculates the diffusive flux. It then finds the tortuosity using (1.5) [24]. The other method of flux-based calculation is to use a finite element method to calculate the heat flux through the porous phase using an arbitrary heat transfer coefficient. By comparing the heat flux through the porous matrix to the heat flux through an equivalent solid cube, they found the tortuosity factor in a similar form to (1.5) [21].

As shown in Figure 1-9, TauFactor and the heat flux simulation produce remarkably similar results. TauFactor offers the distinct advantage of automatically meshing the image directly from the voxels in the input image [24]. This eliminates the arduous step of manually meshing the image that is required for the heat flux method.

Tjaden et al. compared the results of their simulations with their experiments and found that the experimentally derived tortuosity is higher than the tortuosity predicted using either of the imaging techniques (Figure 1-9). They hypothesize that Knudsen effects,

which are not accounted for in any of the image processing algorithms, may be contributing significantly to the retardation of the diffusion [20].

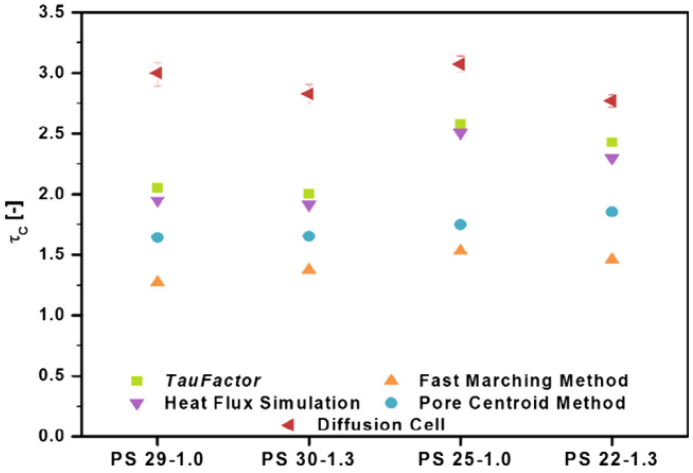

Figure 1-9 Comparison of geometric (Fast Marching Method, Pore Centroid Method), Flux-based simulation (TauFactor, Heat Flux Simulation), and Experimental (Diffusion Cell) Tortuosity for four different samples [20]

2 Tomography Theory

2.1 *Chapter Introduction*

X-ray computed tomography (CT) is a non-destructive imaging technique that allows for the micro and nano scale study of material morphology in three dimensions. This gives it a distinct advantage over other methods such as focused ion beam scanning electron microscopy (FIB-SEM) which is a destructive technique, and transmission electron microscopy (TEM), which can also be used with rotation to produce tomographs, however it is limited to thin samples, on the order of 100 nm [3]. FIB-SEM and TEM techniques rely on electron beams for imaging, which enables them to image with higher resolution than x-ray techniques, however x-rays can image materials of higher densities. There are two methods of x-ray imaging described in this paper: absorption contrast imaging and phase contrast imaging. This chapter provides an overview of these

techniques, starting with the optical theory upon which they are built. From there, a useful guide to choosing the correct imaging technique based on the material being studies is presented. Finally, x-ray absorption near edge spectroscopy (XANES) is discussed. XANES is a technique that may be combined with many x-ray imaging techniques to explore the chemical makeup of a material based on its absorption spectra as a function of x-ray energy.

2.2 *Optics Theory*

2.2.1 Free Space Wave Equation

The electric field of an x-ray travelling in free space in the z-direction is described using the wave equation (2.1).

$$E(z,t) = E_0 \exp(j(k_0 z - \omega t)) \tag{2.1}$$

$$k_0 = \omega / c \tag{2.2}$$

Where E is the electric field, j is the imaginary unit, k_0 is the free space wave number, ω is the angular frequency of the wave, t is time, and c is the speed of light in a vacuum [25, 26]. The wavenumber is a convenient way of expressing the wavelength or energy of a wave. These terms are related in equation (2.3).

$$k_0 = \frac{\omega}{c} = \frac{2\pi}{\lambda} = \frac{E}{\hbar c} \tag{2.3}$$

Where λ is the wavelength, E is the photon energy, and $\hbar$ is the reduced Planck constant. It should be noted that an alternate convention for (2.1) exists and is given by (2.4).

$$E(z,t) = E_0 \exp(-j(k_0 z - \omega t)) \tag{2.4}$$

The convention defined in (2.1) is more common in the physics community and is used in most optics textbooks. The convention defined in (2.4) is more common in the

engineering community and is used in most tomography data sources such as the Lawrence Berkeley National Laboratory (LBNL) X-Ray Data Booklet [27]. For the sake of completeness, this paper will address both conventions and will refer to them as the physics and engineering conventions respectively.

2.2.2 Refraction

When light strikes a non-absorbing surface, it is refracted due to the differing speeds of light in the medium compared to the surroundings as described by Snell's law

$$\frac{\sin\theta_i}{\sin\theta_t} = \frac{v_1}{v_2} = \frac{n_2}{n_1} \tag{2.5}$$

$$n = c / v \tag{2.6}$$

Where θ is the angle relative to the normal of the surface, *i* refers to the incident wave, *t* refers to the transmitted wave, *v* is the speed of light in the medium, *c* is the speed of light in a vacuum, and *n* is the refraction index [26]. The free space wave number k_0 is based on the speed of light in a vacuum (2.7). Since the speed of light in a medium differs from that in a vacuum, the free space wave number must be replaced in (2.1) with the wave number based on the speed of light in that medium (2.8) to form (2.9).

$$k_0 = \omega / c \tag{2.7}$$

$$k = \omega / v = k_0 n \tag{2.8}$$

$$E(z,t) = E_0 \exp(j(k_0 n z - \omega t)) \tag{2.9}$$

When light passes a distance l through two dissimilar media with refraction indices n_1 and n_2, the light that travelled through the second media will be phase shifted relative to the first by $k_0 n_1 l - k_0 n_2 l$ radians. This is the principle upon which phase contrast imaging is built. The phase difference between the light that travelled through the sample and the

light that travelled around the sample through the air can be measured very accurately through the use of a Zernike phase contrast as illustrated in Figure 2-1.

2.2.3 Absorption

In order to account for the x-rays absorbed by a sample, the refractive index n is replaced with the complex refractive index $\hat{n}$, for which there are four different conventions (2.10)(2.11)(2.12)(2.13).

$$\hat{n} = n(1 + j\kappa) \tag{2.10}$$

$$\hat{n} = n(1 - j\kappa) \tag{2.11}$$

$$\hat{n} = n + j\kappa \tag{2.12}$$

$$\hat{n} = n - j\kappa \tag{2.13}$$

Where $\hat{n}$ is the complex refractive index, n is the real refractive index defined in (2.6), and κ is the attenuation index (also called the extinction coefficient). Equations (2.10) and (2.12) follow the physics convention, whereas (2.11) and (2.13) follow the engineering convention. Additionally, some sources define κ with n built in (2.12)(2.13) [26] and some do not (2.10)(2.11) [25]. It should be noted that this difference does not change the value of $\hat{n}$. In order to avoid confusion, most x-ray references present $\hat{n}$ as follows:

$$\hat{n} = 1 - \delta + j\beta \tag{2.14}$$

$$\hat{n} = 1 - \delta - j\beta \tag{2.15}$$

Where δ is the refractive index decrement and β is the absorption index. This convention aligns better with that used in (2.12) and (2.13), so they will be used for the remained of this paper. It should be noted that δ is a positive number in the x-ray energy range, which implies that the speed of light is faster in the medium than in a vacuum. This does not

violate the theory of relativity as the information is still travelling slower than c [28]. The relativistic implications of this are beyond the scope of this work. Equation (2.14) follows the physics convention and (2.15) follows the engineering convention. δ and β are derived from fundamental quantities and the complex atomic scattering factor.

$$\delta + \beta = \frac{r_e}{2\pi}\lambda^2 \sum_i n_i f_i(0) \tag{2.16}$$

$$f(0) = f_1 + jf_2 \tag{2.17}$$

Where r_e is the classical electron radius, λ is the wavelength, n_i is the number of atoms of type *i* per unit volume (also known as the mass density), and *f* is the complex atomic scattering factor (also known as the atomic form factor) which is a function of photon energy. The atomic scattering factor may be found tabulated in numerous physics sources, such as those published by the National Institute of Standards and Technology (NIST) [29]. LBNL provides an online calculator for δ and β for both elements and compounds at various photon energies as part of the supplemental material to their X-Ray Data Booklet [27].

2.2.4 Intensity

The complex attenuation coefficient (2.12) can be substituted into the electric field equation (2.9) to account for both attenuation and phase shift (2.18). The magnetic field can be expressed in the same manner (2.19).

$$E(z,t) = E_0 \exp\left(-\frac{\kappa\omega z}{c}\right)\exp\left(j\left(k_o n z - \omega t\right)\right) \tag{2.18}$$

$$H(z,t) = H_0 \exp\left(-\frac{\kappa\omega z}{c}\right)\exp\left(j\left(k_o n z - \omega t\right)\right) \tag{2.19}$$

$$\sqrt{\mu}H_0 = \sqrt{\epsilon}E_0 \tag{2.20}$$

Where H is the magnetic field, μ is the magnetic permeability, and ε is the dielectric constant. The first exponential term accounts for the decrease in field strength due to the attenuation. The second exponential term accounts for the phase shift discussed previously [25]. It should be noted that x-ray detectors measure the intensity of light, not the electromagnetic field, which is given by (2.21).

$$I = \frac{c}{8\pi}\left|Re\left\{E \times H^{*}\right\}\right| \tag{2.21}$$

Where I is the intensity, E is the electric field, H is the magnetic field, and * denotes the complex conjugate [26]. Substituting (2.18) and (2.19) into (2.21) yields an expression for the intensity of the light, (2.22), which is time independent.

$$I(z,t) = \frac{c}{8\pi} H_0 E_0 \exp\left(-\frac{2\kappa\omega z}{c}\right) \tag{2.22}$$

This relation is known as the Beer-Lambert Law, and is usually expressed in the form shown in (2.23).

$$I(z) = I_0 \exp(-\mu z) \tag{2.23}$$

$$\mu = \frac{2\kappa\omega}{c} = 2k_0\kappa = 2k_0\beta \tag{2.24}$$

Where μ is the attenuation coefficient (also known as the absorption coefficient) which is in units of length^{-1} (most often cm^{-1} however μm^{-1} and nm^{-1} are also used). Physics texts tend to use α instead of μ to express the attenuation coefficient. It should be noted that the quantity in the first exponential term of (2.18) is equal to $\mu/2$ because the intensity is proportional to the electric field strength squared. The Beer-Lambert law is the most common way of describing the intensity drop between two points and can be generalized to cases where the absorption coefficient varies in space as shown in (2.25) [26].

$$I = I_0 \exp\left(-\int_{P1}^{P2} \mu(z)dz\right) \tag{2.25}$$

The attenuation coefficient is often tabulated as the mass attenuation coefficient. This alters the form of (2.23) to (2.26).

$$I(z) = I_0 \exp(-(\mu/\rho)x) \tag{2.26}$$

$$x = \rho l \tag{2.27}$$

Where μ/ρ is the mass attenuation coefficient in cm^2g^{-1}, x is the mass thickness of the material, ρ is the density of the material, and l is the thickness [29]. For compounds, the mass attenuation coefficient can be calculated using (2.28).

$$\mu/\rho = \sum_i w_i(\mu/\rho)_i \tag{2.28}$$

Where w_i is the weight fraction of the i^{th} atomic constituent [29].

2.2.5 Interference

When two waves are superimposed, their electric and magnetic fields are summed (2.29).

$$E = E_1 + E_2 \tag{2.29}$$

Since the magnetic field is related to the electric field by a constant (2.20), its contribution will be implied. The intensity (2.30) is therefore proportional to the square of the electric field, which is given by (2.31).

$$I = I_1 + I_2 + J_{12} \tag{2.30}$$

$$E^2 = E_1^2 + E_2^2 + 2E_1 \bullet E_2 \tag{2.31}$$

Where J_{12} is the interference term. Derivation of this formula requires expressing the electric field (2.32) in terms of its complex amplitude (2.33).

$$E(z,t) = \mathrm{Re}\{A(z)e^{-j\omega t}\} = \frac{1}{2}\left[A(z)e^{-j\omega t} + A^*(z)e^{j\omega t}\right] \tag{2.32}$$

$$A(z) = E_0 \exp(jk_0 nz) \tag{2.33}$$

Where A is the complex amplitude, E_0 is its magnitude and the term inside the exponential is its phase. The interference term is therefore

$$J_{12} = 2E_1 \bullet E_2 = \frac{1}{2}(A_1 e^{-j\omega t} + A_1^* e^{j\omega t}) \bullet (A_2 e^{-j\omega t} + A_2^* e^{j\omega t}) \tag{2.34}$$

Which reduces to

$$J_{12} = \frac{1}{2}(A \bullet B^* + A^* \bullet B) \tag{2.35}$$

Substituting (2.33) into (2.35) yields

$$J_{12} = E_{0,1} E_{0,2} \cos(k_0 n_1 l - k_0 n_2 l) \tag{2.36}$$

The total intensity is usually written as

$$I = I_1 + I_2 + 2\sqrt{I_1 I_2} cos(\phi) \tag{2.37}$$

Where ϕ is the term inside the cosine in (2.36), also known as the phase shift between the two waves. The Beer-Lambert law (2.23) can be used to calculate reduction in intensity due to attenuation. The reduced intensities can then be used in (2.37).

2.3 *Application to X-ray Tomography*

Both the human eye and photo detection equipment can only measure light intensity. This is ideal for absorption contrast imaging which relies on the decrease in light intensity due to attenuation. For phase contrast imaging, this is a problem as it means there is no way to measure the phase of the light directly. Zernike developed the phase contrast method in 1935 to produce an attenuation drop that is directly proportional to the phase shift. For this, he was awarded the 1953 Nobel Prize in Physics [26].

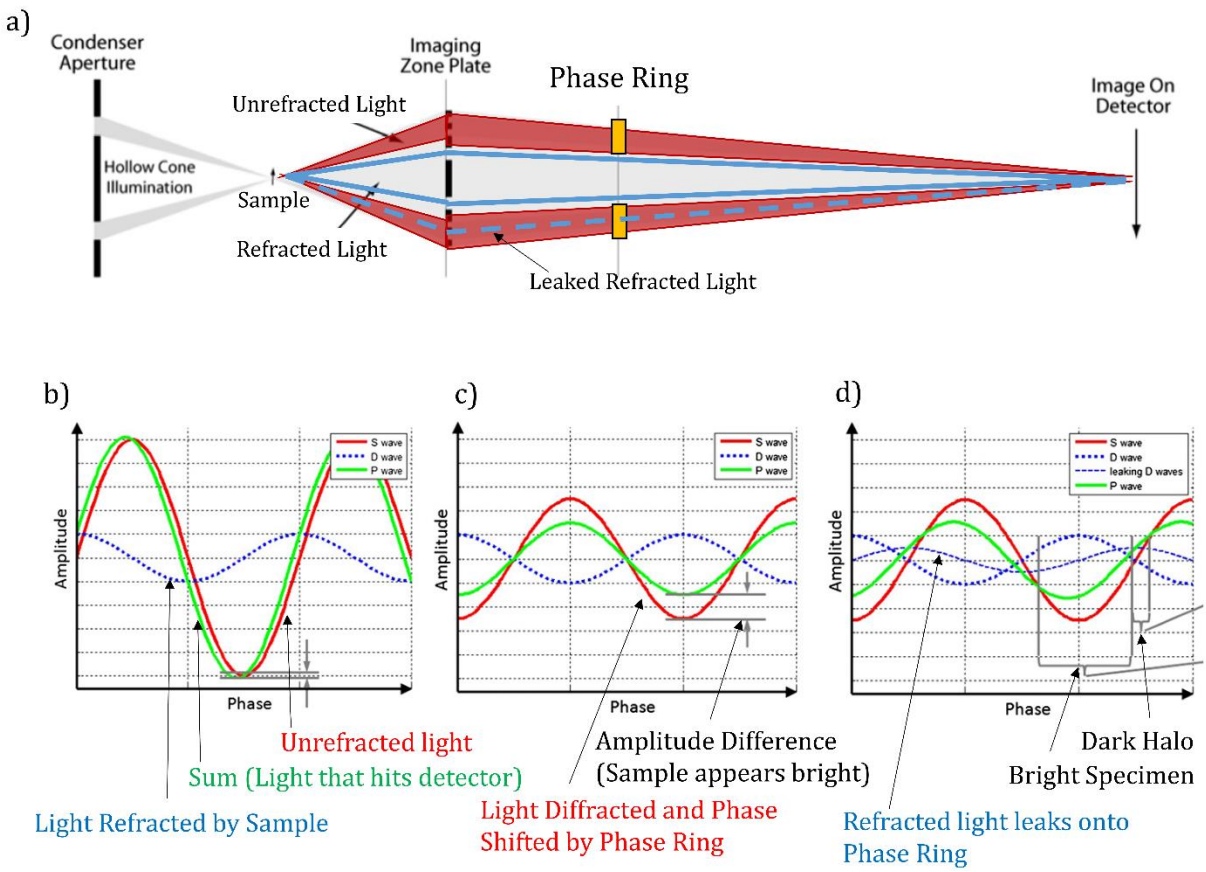

Figure 2-1. Zernike phase contrast imaging a) diagram of phase ring placement [30] b) absorption contrast imaging c) phase contrast imaging (ideal) d) phase contrast imaging (real) [31]

Zernike phase contrast uses a condenser to focus a hollow cone of monochromatic x-rays on the sample as seen in Figure 2-1a. The light that travels around the sample is unrefracted and represented in red. The light that strikes the sample is refracted and attenuated and represented in blue. The light then reaches the zone plate which diffracts it to focus it on the image detector. Refraction is the bending of light that strikes the surface of a material with a different speed of light than the one it had been traveling through and is described by Snell's law (2.5). Diffraction is the bending of light as it passes through a slit that is smaller than the wavelength of the light. In the case of absorption contrast

imaging, the phase ring is not present and the x-rays incident on the detector are described by Figure 2-1b. For weakly attenuating specimens, the signal from the light that goes through the sample (blue) is not sufficiently different from the light that goes around the sample (red) to noticeably affect the light hitting the detector (green). The phase ring shown in Figure 2-1c attenuates the unrefracted light (red) and phase shifts it by $\pi/2$. When this attenuated and phase shifted signal is combined with that from the sample, the two signals exhibit destructive interference, as described by (2.37). This interference reduces the intensity of light hitting the detector, making the sample show up brightly (since the color contrast is inverted upon reconstruction). The interference is highly dependent on the phase of the refracted light (blue) which gives Zernike phase contrast its high sensitivity.

One problem with Zernike phase contrast is when diffracted light leaks onto the phase ring. This can happen when the beam strikes a feature at an angle greater than the critical angle for total internal reflection and is then reflected towards the unrefracted light. This is illustrated in Figure 2-1d, the leaked refracted light is phase shifted and attenuated by the phase ring and interferes with the signal causing dark halos around the edges of features. Numerous image processing algorithms have been proposed to reduce the effects of these halos such as those by Yin et al. [31].

2.4 *Guide to use theory for experiment design to predict effectiveness of phase vs absorption-contrast imaging*

In absorption contrast imaging, the brightness of an object in the reconstructed image is inversely proportional to its attenuation, since the reconstruction algorithm inverts the color contrast. The attenuation can be predicted with the Beer-Lambert law (2.38).

$$I = I_0 \exp(-\mu l) \tag{2.38}$$

$$\mu = 2k_0\beta \tag{2.39}$$

The attenuation is dependent on the thickness of the material *l*, and the attenuation coefficient μ which can be determined by consulting the tabulated value of β at the photon energy being used.

Phase contrast imaging relies on the phase shift of the wave that travels through the sample relative to the wave that travels through the air around the sample. This phase shift can be predicted using (2.40), and the corresponding attenuation drop by (2.41).

$$\phi = k_0(1-\delta_{air})l + \frac{\pi}{2} - k_0(1-\delta)l \tag{2.40}$$

$$I_{detector} = I_0 + I + 2\sqrt{I_0 I}cos(\phi) \tag{2.41}$$

Where $I_{detector}$ is the intensity of light incident on the detector, *I* is the intensity of light after passing through the sample (calculated using the Beer-Lambert Law (2.38)), I_0 is the intensity of light that went around the sample (assuming no attenuation from the air), ϕ is the phase shift in radians and *l* is the thickness of the material. It should be noted that the relationship between the calculated attenuation of an object and its brightness in the reconstructed image may not be linear, as the contrast of the image must be adjusted in order to be seen with the human eye. X-ray absorption near edge spectroscopy (XANES) relies on exact values of the intensity incident upon the detector, and will be discussed presently. Equations (2.38) and (2.40) are most useful in predicting which components will show up most brightly in an image. Figure 2-2 shows various x-ray properties of some common fuel cell membrane components in order to demonstrate this. The x-axis range corresponds to typical tender and hard x-rays range used in x-ray CT.

Synchrotron sources allow for varied energy range, however lab-scale x-ray CT machines are generally fixed to single energy value.

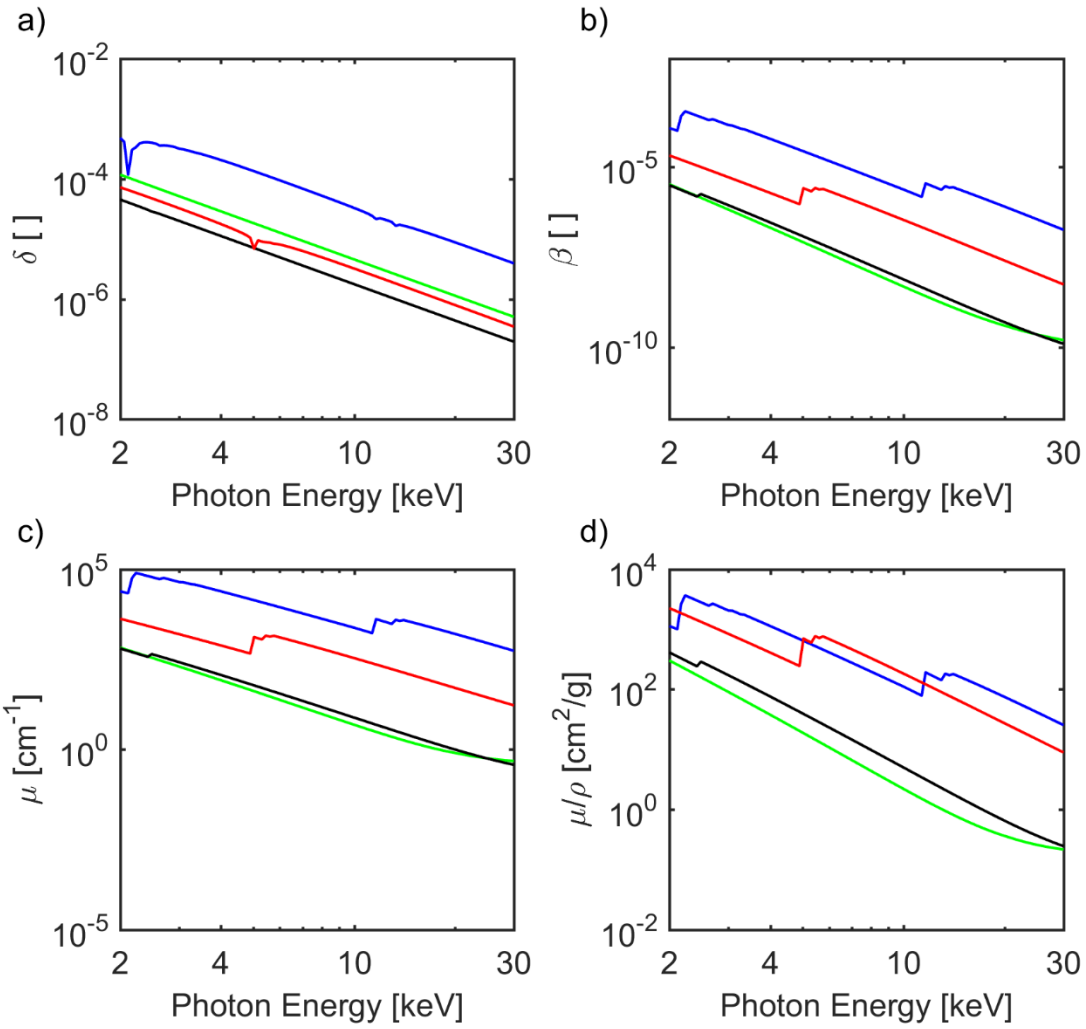

Figure 2-2. Various optical properties of Platinum (Blue), Cesium (Red), Carbon (Green), and Nafion Ionomer (black) as a function of photon energy. a) Refractive index decrement (δ) b) absorption index (β) c) attenuation coefficient (μ) d) mass attenuation coefficient (μ/ρ)

Since the thicknesses of various components within a sample tend to vary by less than an order of magnitude, the attenuation and phase shift are stronger functions of δ and β.

Figure 2-2a shows that the features in order of decreasing brightness in phase contrast will be Platinum (Pt), Carbon (C), Cesium (Cs), Nafion. Thus, when imaging a composite material including all these four materials, Pt will be fairly easy to separate, whereas C, Cs and Nafion will have similar brightness. Figure 2-2b shows that in absorption contrast, the order will change to Pt, Cs, Nafion, C, which is directly proportional to material's atomic number. These graphs can be useful in selecting the appropriate imaging technique to study a specific material. It should be noted that while weakly attenuating objects (such as C in the above plots) are very difficult to see in absorption contrast imaging, weakly phase shifting objects are still visible in phase contrast imaging. This is due to the fact that modern phase rings make it possible to detect minute changes in phase. This makes phase contrast imaging ideal for imaging weakly absorbing features.

2.5 *XANES Imaging*

X-ray absorption near edge spectroscopy (XANES) is a technique that can be combined with various forms of X-ray CT to provide chemical information. This technique is a subset of a more general technique called x-ray absorption spectroscopy (XAS). XANES focuses on interpreting data at energies near an absorption edge of a material, whereas XAS considers the full spectrum. XANES consists of scanning a sample at multiple photon energies in order to take advantage of absorption edges [32]. Unlike tomography images, in which brightness is proportional to the intensity of light, but are not mapped linearly, XANES measures the intensity of light on the detector exactly. Using the Beer-Lambert Law, and the known intensity of the non-attenuated light, the attenuation of the sample is reported in the form of the optical depth (2.42) (also known as the optical

thickness). The optical depth is the term inside the exponential in the Beer-Lambert law (2.38).

$$\tau = \mu l = \int_0^l \mu dz \tag{2.42}$$

The optical depth (τ) is calculated across the width of the entire sample (l) where the attenuation coefficient (μ) changes along the width of the sample as the x-ray passes through different constituent materials. XANES chemical mapping usually consists of scanning the sample at an array of discrete energies below and above the absorption edge of the substance being studied. Figure 2-3 shows this process for a dispersed nickel-copper (NiCu/KB) sample on carbon support (Ketjen Black). The nickel (Ni) K-edge is located at 8.33 keV (Figure 2-3a) and has a width of 1.44 eV [27], so the sample was scanned between 8.3 and 8.5 keV in 1 eV steps. The average optical depth across the area of the radiograph is plotted for each energy. The spike at 8.34 keV shows the presence of Ni in the sample, since the attenuation spiked at the Ni edge.

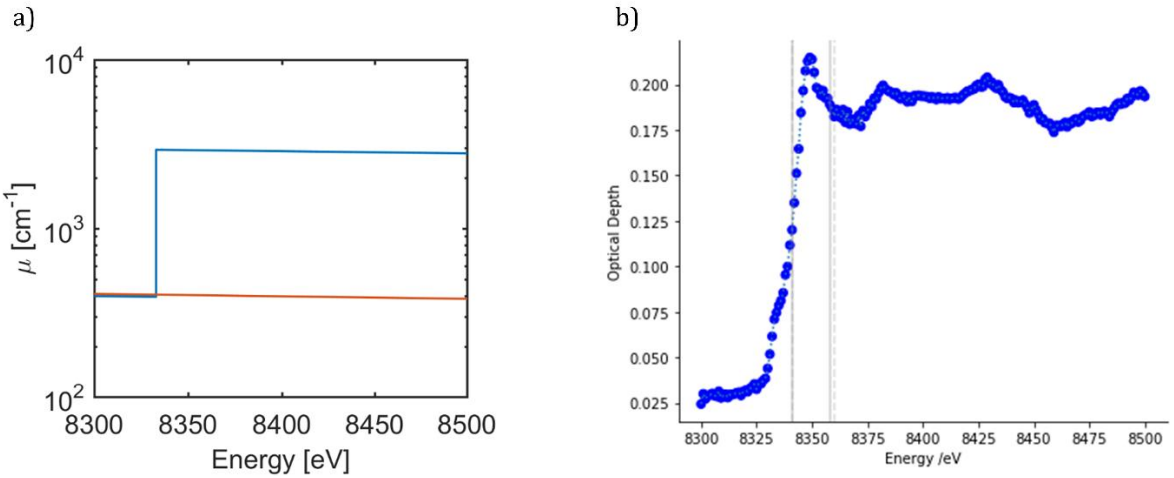

Figure 2-3. a) Ni (blue) and Cu (red) attenuation coefficients b) optical depth as a function of photon energy for a NiCu sample about Ni edge

Absorption edges are the spikes in the absorption index (and by extension the attenuation an mass-attenuation coefficients) (Figure 2-2) caused by electrons becoming photoexcited at discrete frequencies [25, 33]. Another way XANES takes advantage of this phenomenon by scanning at energies above and below an absorption edge and comparing the two images to isolate the desired component. This technique is known as two energy imaging. XANES is a useful technique in many fields, as it also allows the determination of oxidation states of materials. In the energy field, it has been used for various operando experiments such as those by Weker et al. [32] for the mapping of local oxidation state of cathodes in Li-ion batteries.

2.6 *Chapter Conclusion*

Understanding the physics behind x-ray CT is critical to its proper use. The ability to predict the attenuation through a material of known thickness will be critical in the design of the micro and nano CT fuel cells in Chapters 5 and 6. Knowledge of which materials will appear most brightly in the reconstructed image helps both in the selection of imaging techniques, but also in the analysis of the resultant image. Furthermore, the combination of XANES and nano-CT is a powerful technique as it accounts for both morphological and chemical information and will be discussed in terms of applications in Chapter 6.

3 Platinum Loading and Distribution

3.1 *Chapter Introduction*

Platinum (Pt) is the most expensive component of the fuel cell stack, making up about 40% of the total cost [34]. As a result, manufacturers have made several attempts to reduce the Pt loading of fuel cell catalysts while maintaining their performance. Pt

catalyzes the both the anode hydrogen oxygenation reaction (HOR) (3.1) and the cathode oxygen reduction reaction (ORR) (3.2).

$$2H_2 \rightarrow 4H^+ + 4e^- \quad (3.1)$$

$$O_2 + 4H^+ + 4e^- \rightarrow 2H_2O \quad (3.2)$$

Of the two reactions, the ORR has the more sluggish kinetics, requiring more electrocatalyst. The caveat is that the reaction takes place on the surface of the Pt particle [35]. This means that the optimal design for the electrode is one that has the highest surface area to volume ratio of Pt. Although not all these designs are stable or are able to maintain activity during durability cycling, the entire series of designs is presented in order to better gauge the relationship between design parameters and Pt distribution. The catalyst layer of a state of the art fuel cell is prepared as an ink consisting of carbon black (CB), Pt nanoparticles, and ionomer, which is deposited onto the membrane by one of various inject printing, spraying or blade casting methods. The CB acts as a support material, the platinum acts as the reaction electrocatalyst, and the ionomer acts as both the binder and the electrolyte through which the protons conduct [35, 36]. The proportions of these three ingredients in the ink play a critical role in their performance, as does the catalyst layer morphology. The catalyst layer morphology has to accommodate the transport of electrons (via CB), protons (via ionomer) and oxygen reactant (via pore space), at the same time ensuring that the byproduct—water—can be removed from the catalyst layer (also via void space).

3.1.1 Nano-Structured Thin-Film Electrodes

3M has developed a novel class of catalyst layers called nano-structured thin-film electrodes (NSTFs)[36-39]. NSTF electrodes have pyrelene red as support material that is

highly porous and shaped as vertically-standing whiskers. Onto these whiskers Pt catalyst is deposited in a roll-to-roll process via sputtering. NSTF electrodes do not use ionomer or carbon. These electrodes met the activity and durability standards prescribed by Department of Energy, however struggled to meet robustness standards. The robustness test involves operating the fuel cells at lower temperatures (40°C, as opposed to the typical 80°C), while maintaining 70 % of the standard temperature power density. NSTF electrodes are very thin (~0.5 um in thickness) compared to conventional catalyst layers (~10 um thick) and have a large local flux of water, as production of water is proportional to current density. At lower temperatures evaporative removal of water is suppressed [14], resulting in flooding. To resolve the issue of layer thickness and associated robustness, 3M came up with a concept of dispersed NSTF, or dNSTF. This electrode design combines the advantages of a conventional layer with that of NSTF electrodes. The whiskers that are 0.5 - 1 um in length and 50 nm in diameter are shaved off of the liner and then mixed with carbon and ionomer to form ~10 um thick catalyst layers.

The weight ratio of Pt/pyrelene whiskers to CB is known as the whiskers to carbon ratio (Wh/C) and is a key component to optimize to ensure proper catalyst layer design. The weight ratio of the ionomer to the CB is known as the ionomer to carbon ratio (I/C). This study examines catalyst inks of varying Wh/C on two different CBs – medium surface area carbon and high surface area carbon. High surface area carbon enables better Pt dispersion but inherently is not as graphitic and hence not as stable during durability or degradation studies.

3.1.2 Ionomer Distribution

It is essential that the ionomer be uniformly distributed as it provides a path for the protons to reach the catalyst sites on the surface of the platinum [35]. For thick electrodes ionomer distribution is even more important because of longer distances that protons have to traverse. Experiments have corroborated this, showing that ionomer loading and distribution both significantly affects performance [40, 41].

In this study, various morphological properties of each catalyst layer are compared to analyze their potential strengths and weaknesses. The properties measured include the porosity and tortuosity factor of the carbon matrix, and the volume fraction and agglomerate size distribution of the Pt whiskers. These properties are measured using x-ray nano computed tomography (CT) which was performed at beamline 32-ID-C at the Advanced Photon Source (APS) at Argonne National Laboratory in Lemont, IL. The nano CT imaging has a field of view of 73 μm and a resolution of 30 nm, after binning the image we use 60 nm resolution. This beamline has a range of energies from 8 to 12 keV, however a phase contrast imaging is only possible at 8 keV.

Given the importance of ionomer distribution, there have been several attempts to quantify it using imagining techniques [40, 42]. Ionomer has a low attenuation coefficient, so it will not be visible in absorption contrast imaging (Table 3-1). It also has a refractive index decrement that is lower than both Platinum and Carbon, which means that it will be the dimmest feature on a phase contrast image (Figure 2-2). A solution to this imaging problem is to stain the ionomer with Cesium ions. Cesium has a high

attenuation coefficient (Table 3-1) and therefore shows up brightly in absorption contrast imaging.

Table 3-1. Linear Attenuation Coefficients of Catalyst Components

Material	Linear Attenuation Coefficient at 8 keV – μ (cm^{-1})
Platinum (Pt)	4200
Cesium (Cs)	617
Nafion Ionomer	15
Carbon	9.7

Section 2.4 details the process of selecting an appropriate imaging technique based on the material being studied. This study aims to quantify three parameters of the catalyst layer summarized in Table 3-2.

Table 3-2. Imaging Goals

	Goal	Imaging technique
Platinum distribution	Maximize surface area to volume ratio	Absorption Contrast
Ionomer	Ensure even distribution and that all Pt is in contact with Cs	Cs stain and Absorption Contrast
All solid phase	Flow channels through porous electrode allow	Phase Contrast Imaging

	easy diffusion of O_2 and water	

The use of both absorption and phase contrast imaging on a single sample allows the results of the two to be overlaid.

3.2 *Sample Procedure*

A 2 mm^2 triangle of electrode on liner was cut using a razor blade. The sample was stained by soaking it in a saturated Cesium chloride solution for 24 hours. The sample was then rinsed with deionized water, and allowed to dry which left behind Cs+ stained ionomer. It was then epoxied to a 0.3 mm diameter tungsten pin for imaging. The staining procedure poses a significant challenge as rinsing the sample too much causes the Cs+ ions to diffuse out of the ionomer, however not rinsing the sample enough leaves large Cs crystals at the edge of the sample. These crystals appear so brightly in the reconstructed image that it is difficult to see any other features.

The sample was then scanned at APS beamline 32-ID-C at a photon energy of 8 keV in both absorption and phase contrast mode. The resulting images were then reconstructed into 3D volumes using algorithms within the TomoPy package developed by APS [43].

3.3 *Image Processing*

After using Filtered Back Projection algorithms for reconstructions, a stack of images representing 3D volume is produced. The first step in the image processing procedure is to threshold the images to separate various phases, as shown in Figure 3-2. Thresholding refers to the process of turning a grayscale image into a binary one. Reconstructed 8-bit images have grayscale values ranging from 0 (black) to 255 (white). These grayscale

values are graphed in a histogram, which shows the distribution of grayscale values (Figure 3-1).

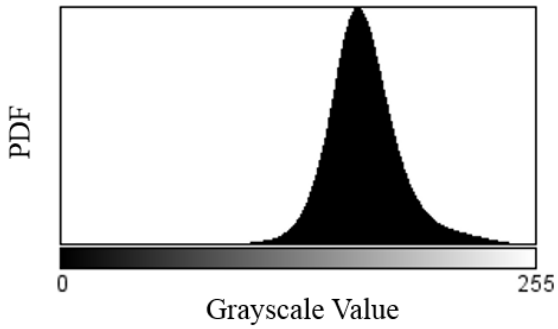

Figure 3-1 Histogram of the image in Figure 3-2c

Once a threshold grayscale value is selected, all pixels with a grayscale value above the threshold are set to white, and all pixels with a grayscale value below the threshold are set to black. There are several algorithms that automatically select the threshold value, perhaps the most famous of which is Otsu's algorithm [44, 45]. The bright platinum is easy to spot with the eye, however sometimes Otsu's algorithm misses it. The best procedure is to therefore use Otsu's algorithm to find a preliminary threshold value, then manually adjust that value to ensure that all of the bright Pt spots are above the threshold.

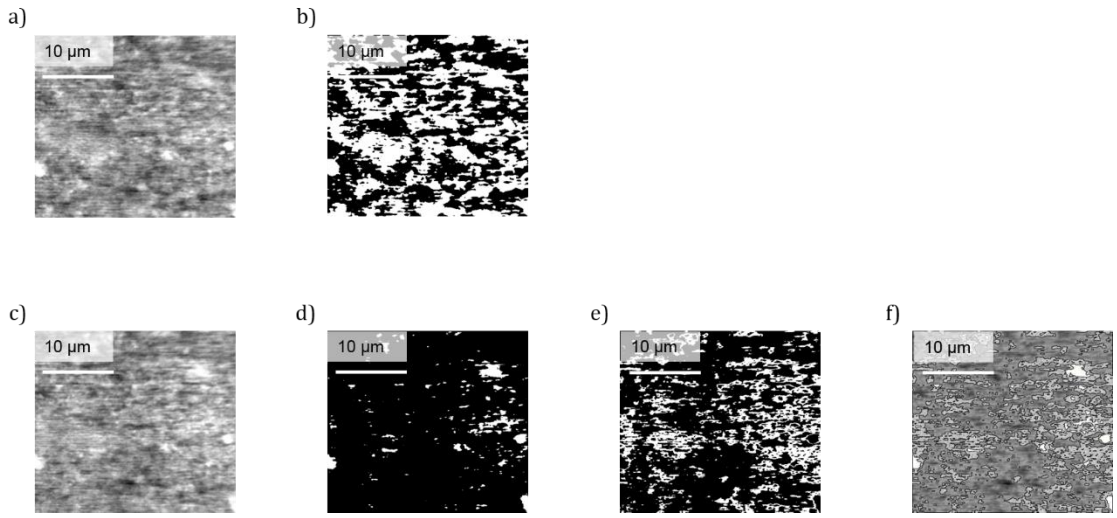

Figure 3-2. Thresholding procedure a) phase contrast image b) thresholded phase contrast image (solid phase white) c) absorption contrast image d) thresholded absorption contrast image (platinum white) e) thresholded absorption contrast image (ionomer white) f) absorption contrast image with ionomer highlighted

The phase contrast image is best for visualizing the entire solid phase (Figure 3-2a). The use of a local thresholding algorithm prevents the bright Pt from overshadowing the less bright carbon (Figure 3-2b). Local thresholding algorithms threshold each pixel based not on the histogram of the entire image as in bulk thresholding, but on the histogram of a group of pixels within N pixels of the pixel in question [44]. This prevents outlier pixels from having an outsized effect on the thresholding of the entire image. If a bulk thresholding algorithm was used, all it would pick up would be the Pt since it is much brighter than anything else. Using a local thresholding algorithm, the more subtle grayscale differences between the carbon and the voids can be easily seen. The absorption contrast image is best for visualizing bright features such as Pt and Cs stained ionomer (Figure 3-2c). Since it has the highest attenuation coefficient, the brightest features in the image are Pt. The threshold is set manually based on the suggested

threshold value from Otsu's method and a rough estimate of the predicted volume fraction based on the Wh/C and the densities of the constituent materials (Figure 3-2d). The same procedure is repeated for the ionomer. The ionomer is easier to threshold since all of the bright features in the image are either Pt or Cs stained ionomer, making them easy to distinguish from the dark carbon. To separate the Pt from the ionomer, the Pt image (Figure 3-2d) is subtracted from the Pt/ionomer image to leave just the ionomer (Figure 3-2e). Finally, in order to present a visual representation of the ionomer distribution, the ionomer image is converted to an outline and overlain on the grayscale image (Figure 3-2f). The thresholded images can also be volume rendered (Figure 3-3).

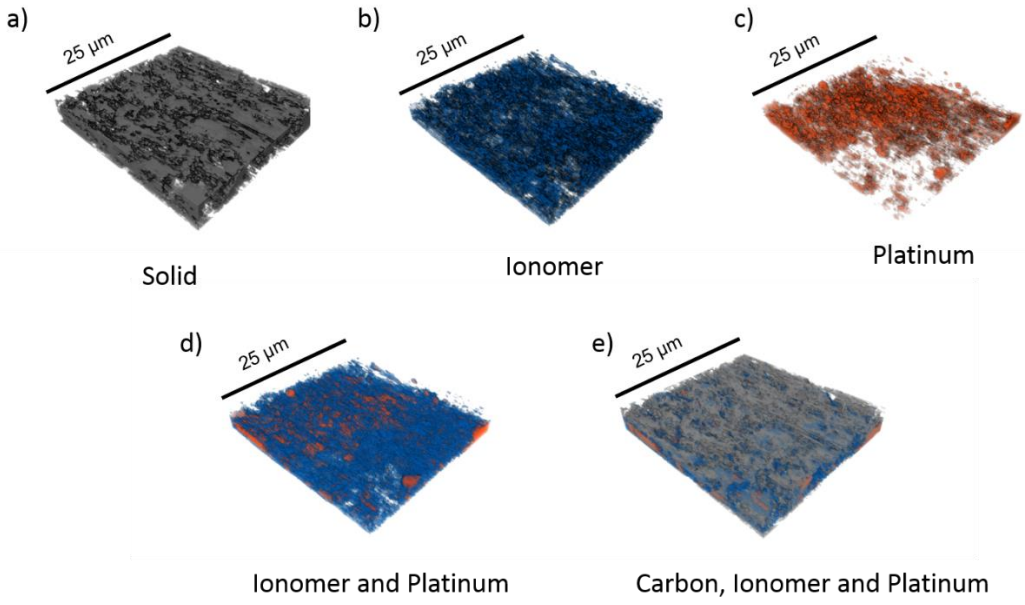

Figure 3-3. Volume renderings of the thresholded images in Figure 3-2 a) all solid phase b) ionomer c) platinum d) ionomer and platinum e) carbon, ionomer and Pt

The method for separating Pt from Cs stained ionomer presented here relies too heavily on educated guess work. Chapter 3 presents a novel method for separating the Pt and ionomer that is far more accurate.

3.4 *Results*

3.4.1 Pt distribution

This process was repeated for two different series of samples, one with medium surface area carbon and a Wh/C range from 2.5 to 50, and one with high surface area carbon and a Wh/C range from 2.5 to 20. The platinum distribution was quantified using thee metrics: volume fraction, average agglomerate radius, and agglomerate size distribution. The latter two were calculated using the BoneJ [46] plugin in the FIJI distribution of ImageJ [47].

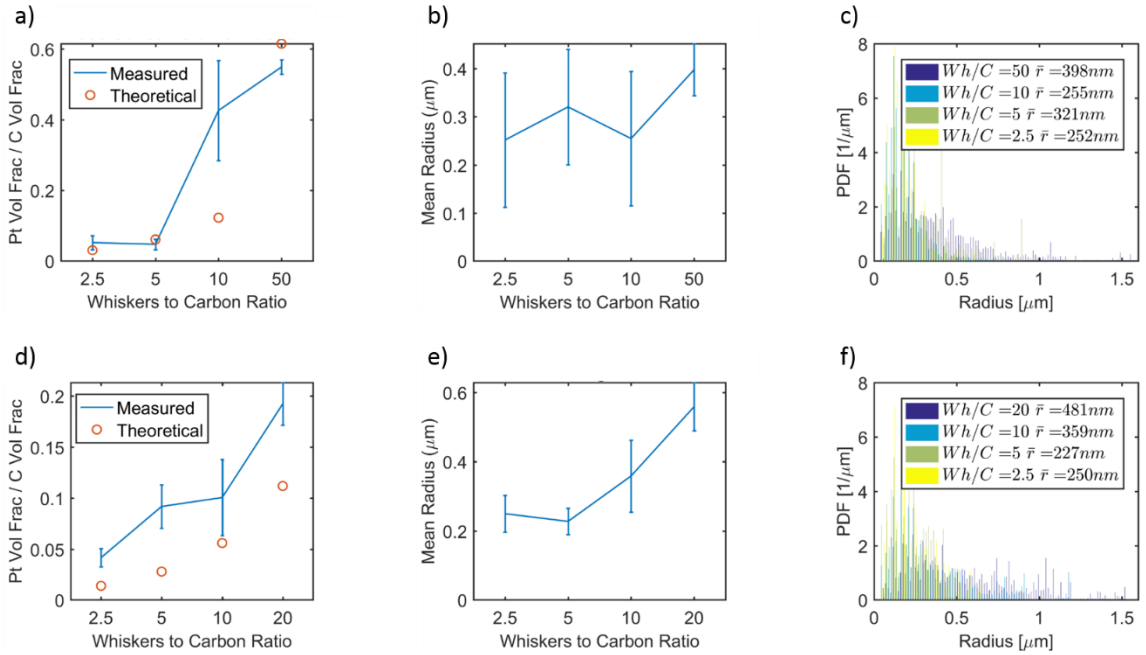

Figure 3-4. Platinum distribution a-c) medium surface area carbon d-f) high surface area carbon a,d) Pt volume fraction vs Wh/C b,e) average Pt agglomerate radius c,f) Pt agglomerate size distribution

The most striking trend is in the average Pt agglomerate radius of the high surface area carbon samples. Above a Wh/C of 10, the Pt forms large agglomerates. The average Pt agglomerate radius of the medium surface area carbons samples is larger than that of the

high surface area carbon samples. Large Pt agglomerates are detrimental to performance as the surface area to volume ratio is inversely proportional to the agglomerate radius.

3.4.2 Porous matrix

The thresholding algorithm used to characterize the porous matrix can have a significant impact on the findings. As discussed previously, local thresholding algorithms base the threshold of each pixel on the histogram of the pixels within a radius of N pixels. N is referred to at the Otsu radius. Figure 3-5 shows the effect of the Otsu radius on the porosity and pore and solid size distribution measurements.

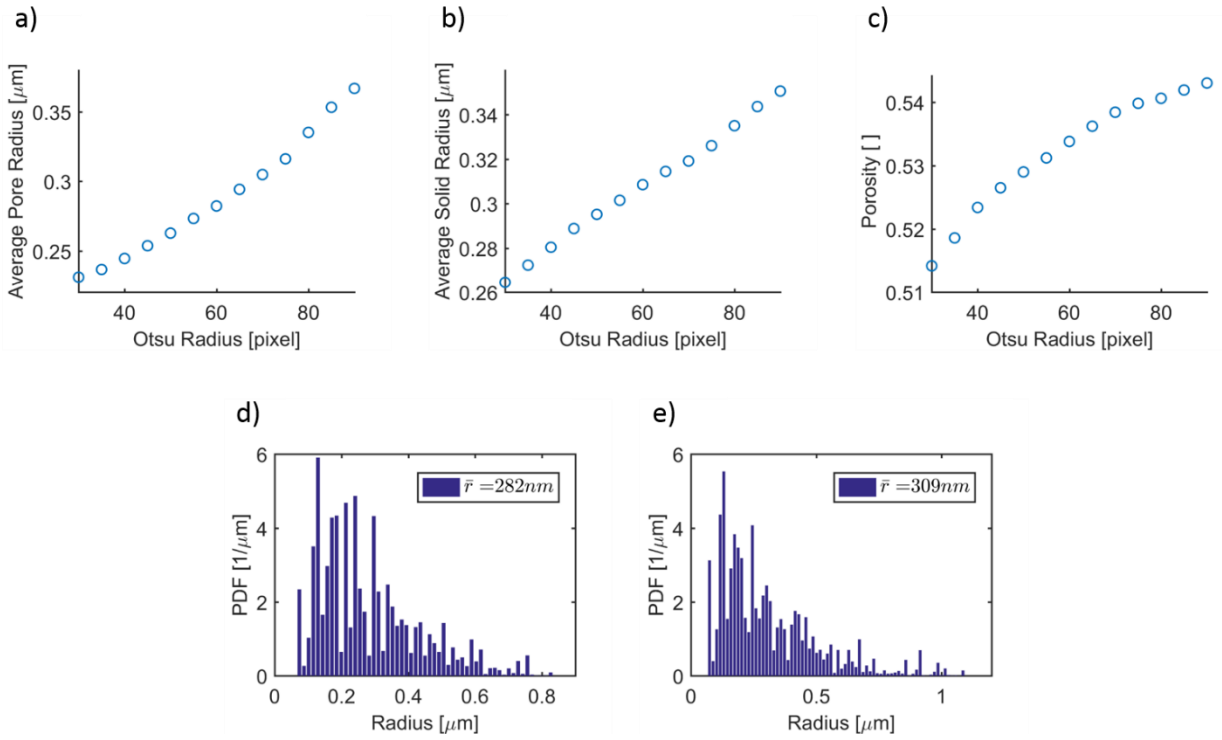

Figure 3-5. Otsu radius effects a) average pore size b) average solid size c) porosity d) pore size distribution and e) solid size distribution for Otsu radius of 60 pixels

Based on this experiment, an Otsu radius of 60 pixels was chosen for the remaining samples. The tortuosity factor was calculated using the Matlab add-in TauFactor [24]. Due to the spraying process by which the catalyst is deposited on the liner, it may have an

orthotropic structure. To account for this, the tortuosity was measured in all three coordinate directions. The two in-plane tortuosities were averaged in order to give a single value for the in-plane tortuosity. This also helped reduce the noise from the reconstruction algorithm which produced some striped artifacts in one of the in-plane directions.

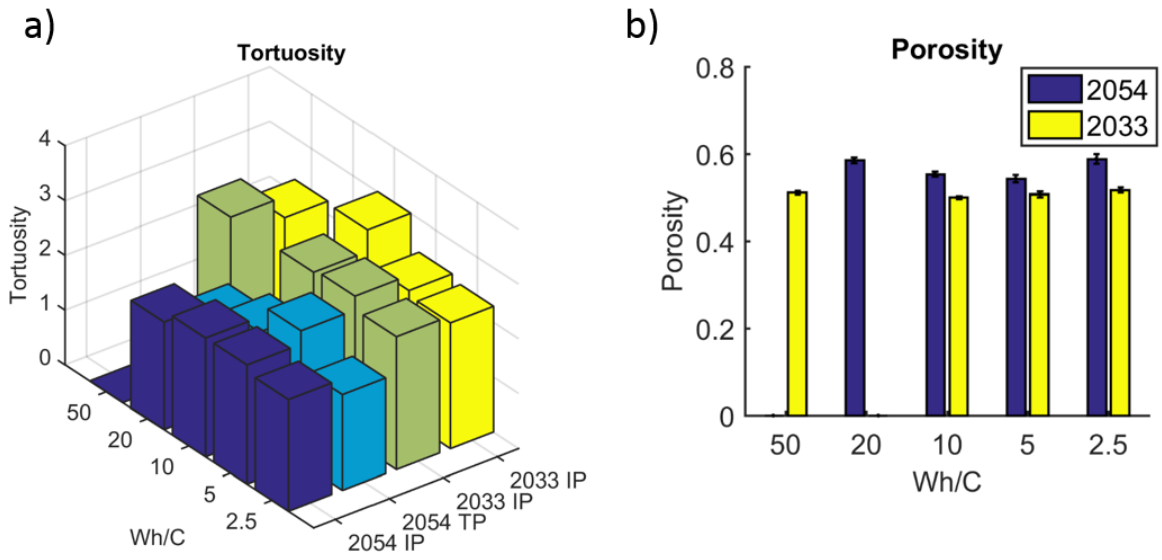

Figure 3-6. Properties of catalysts as a function of Wh/C a) tortuosity factor b) porosity. 2054 refers to high surface area carbon, 2033 refers to medium surface area carbon, IP refers to in plane, and TP refers to thru plane

The tortuosity and porosity studies show that the porous matrix is anisotropic. Additionally, the medium surface area carbon electrodes tend to have a lower porosity and a higher tortuosity factor than the high surface area carbon electrodes. From the catalyst layer design perspective, having higher porosity and lower tortuosity is more desirable, as transport processes will be enhanced in this scenario.

3.5 *Chapter Conclusion*

This chapter presents the study of two series of catalyst electrodes. The Pt on high surface area carbon electrodes were found to form large Pt agglomerates at high Wh/C. The image processing procedure for separating the Pt from the Cs stained ionomer amounted to educated guess work. The next chapter focuses on a novel and much more effective way to separate the Pt and Cs stained ionomer using XANES. The study of the porous matrix of the catalysts showed their anisotropic nature and the dependency of the porosity and tortuosity factor on the carbon type used.

4 Two Energy XANES Imaging

4.1 *Chapter Introduction – Imaging problems with Cs staining*

One method detailed in the previous chapter was the use of cesium (Cs) staining to highlight the ionomer of a catalyst electrode. The problem with that is that both the platinum (Pt) and the Cs have high attenuation coefficients, and will therefore both show up brightly in the reconstructed image. Lopez-Haro et al. [35] used this Cs staining technique for high-angle annular dark-filed scanning transmission electron microscopy (HAADF-STEM). They realized, however, that differentiating between Pt nanoparticles and Cs+ stained ionomer in their images would be impossible, since both features would give high contrast compared to the Carbon black support. Their solution was to prepare a catalyst ink that did not contain any Pt so that they could be sure that all bright features were Cs+ stained ionomer. Using this technique, they were able to show that only 60-76% of the ionomer in the ink ends up uniformly covering the CB support, however they were unable to see how the ionomer interacts with the Pt nanoparticles as they did not include any in their experiments [35]. Others such as Rieberer et al. have also used Cs staining with TEM [48]. Scanning electron microscopy (SEM) is another common way to

study ionomer, although with the drawback that it does not provide 3D imaging, except in the case of focused ion beam SEM (FIB-SEM), which is a destructive technique.

While TEM imaging is useful for visualizing ionomer in 3D, it has a large disadvantage in that the sample must be very thin, on the order of 100 nm [3]. X-ray computed tomography (CT) does not have this limitation and can therefore be used to study the entire thickness of the catalyst layer. X-ray CT is also nondestructive, which makes it much more attractive than FIB-SEM. Kimini Babu et al. [40] demonstrated that Cs staining is an effective method for visualizing ionomer in platinum group metal (PGM) free electrodes using X-ray CT. They avoided the aforementioned challenge of distinguishing between Cs and Pt by using PGM-free electrodes. They found that the ionomer distribution is dependent on loading, with 50 wt% ionomer distributed uniformly and 35 wt% forming large, dense agglomerates.

This paper presents, to the best of the authors' knowledge, the first use of XANES two energy imaging for the separation of Platinum from Cesium stained ionomer in fuel cell catalyst layers.

4.2 *Sample Preparation*

The catalyst ink was prepared as detailed in the supplemental material. A 2 mm^2 triangle of electrode on liner was cut using a razor blade. The sample was stained by soaking in a saturated Cesium chloride solution for 24 hours. The sample was then allowed to dry

which left behind Cs+ stained ionomer. It was then epoxied to a 0.3 mm diameter pin for imaging.

4.3 *Imaging procedure*

The imaging was performed at beamline 6-2 at the Stanford Synchrotron Radiation Lightsource (SSRL) at SLAC National Accelerator Laboratory (SLAC). For each scan, the sample was exposed 180 times for 1 second each as the sample was rotated from 0 to 180 degrees about the axis formed by the pin on which it was mounted. The sample was scanned two times, once at a photon energy of 11.5 keV and again at 11.7 keV. These energies were chosen to take advantage of the L3 absorption edge of platinum as shown in Figure 4-1. At 11.5 keV, the mass attenuation coefficients of Pt and Cs are 80.6 and 136 $cm^2\ g^{-1}$ respectively. At 11.7 keV, they are 191 and 132 $cm^2\ g^{-1}$ respectively. A higher mass attenuation coefficient implies more x-rays are being absorbed; however, this

results in a brighter image because the color contrast is inverted when the image is reconstructed.

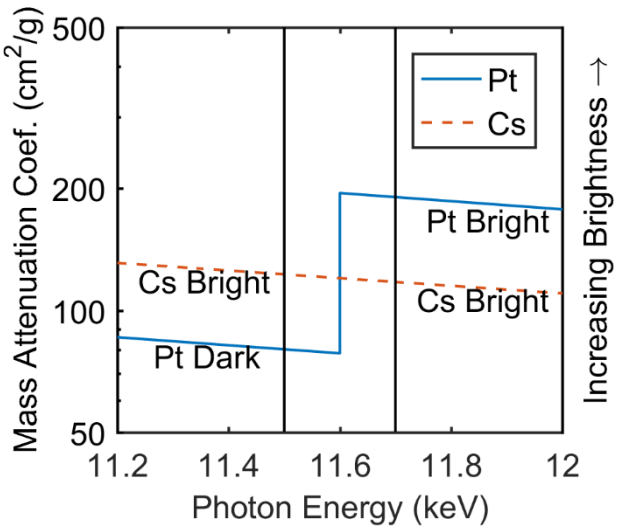

Figure 4-1. Scans were performed at 11.5 and 11.7 keV to take advantage of the Platinum L3 absorption edge

4.3.1 Image processing procedure

The images were reconstructed and aligned using TXM Wizard software [49]. The reconstruction produced images that were 15 x 16 x 24 µm with a voxel size of 24 nm. Once reconstructed, they were cropped using the Fiji distribution of ImageJ [47] to a size of 2.4 x 3.9 x 8.0 µm so that only a pristine section of sample was visible. The 11.5 keV image was then subtracted from the 11.7 keV image. Once the subtraction was complete, all three images were thresholded using a combination of ImageJ's default thresholding algorithm and manual adjustments as detailed in the discussion below. The thresholded images were then analyzed to find the volume fraction and tortuosity factor using Tau

Factor [24], and the size distribution using the BoneJ plugin in ImageJ [46]. Finally, the images were volume rendered using Avizo (FEI Visualization Sciences Group, Berlin).

4.4 *Results/Discussion*

4.4.1 Image processing discussion

The catalyst ink when dried is composed of 32 wt% Nafion ionomer, 34 wt% carbon black, and 34 wt% Pt. Using the densities of the constituent components, a rough estimate for the volume fraction of each phase may be formulated as 54% ionomer, 42% CB, and 4% Pt. While these estimates are not sound enough to derive any meaningful conclusions, they are useful to give a general sense of the proportions of constituent materials in a representative volume. This serves as a way to check the validity of the thresholding.

4.4.2 Separating Pt from Cs

The use of two-energy imaging results in two reconstructed images. The high-energy (11.7 keV) scan shows Pt and Cs as bright, whereas the low-energy (11.5 keV) scan shows Cs only as bright. While the 11.5 keV scan does still pick up the Pt, it is much darker than in the 11.7 keV scan and can be excluded by setting the threshold correctly. First, the default algorithm was used to find a preliminary threshold value. This volume fraction above the threshold was then compared to the theoretical prediction for volume fraction of the phase being isolated. This can be done by considering the above calculations, and by comparing the histograms of the high and low energy images. The threshold value was then adjusted accordingly. There are two possible ways to separate the Pt from the Cs using image subtraction. The first is to subtract the 11.5 keV image from the 11.7 keV image and then threshold all three images. The second is to threshold

the two original images first and then subtract the thresholded 11.5 keV image from the thresholded 11.7 keV image. In the case of the material imaged in this paper, both method were tried, and the first procedure produced results that were much more in line with predictions. The difference image was thresholded in a manner similar to the other two images. The second procedure produced a volume fraction of Pt that was excessively high, owing in large part to the fact that it has a tendency to amplify any salt and pepper noise that may be present in the image. This noise can be reduced using an open (erosion followed by dilation) process, however this process also alters the regions of interest and should be avoided if another alternative exists.

4.4.3 Importance of separating Pt from Cs

Most imaging methods cannot discern between Pt and Cs+ stained ionomer. Since the Pt is very dense, a Pt loading of 34 wt%—as is the case for this sample—yields a relatively low volume fraction of Pt. This leads many to assume that grouping the Pt with the Ionomer will not severely affect the results. Figure 4-2 shows how this assumption can be misleading. Figure 4-2a is taken at 11.7 keV where both Pt and Cs are visible. The bright spot indicated by the arrow could Pt, Cs or a combination thereof. Figure 4-2b is taken at 11.5 keV where only Cs is visible. By subtracting Figure 4-2b from Figure 4-2a, Figure 4-2c shows that the upper part of the bright spot is Pt and the lower part is Cs stained

ionomer. Importantly, this shows that the Pt agglomerate is in contact with the ionomer, which is necessary for ion accessibility.

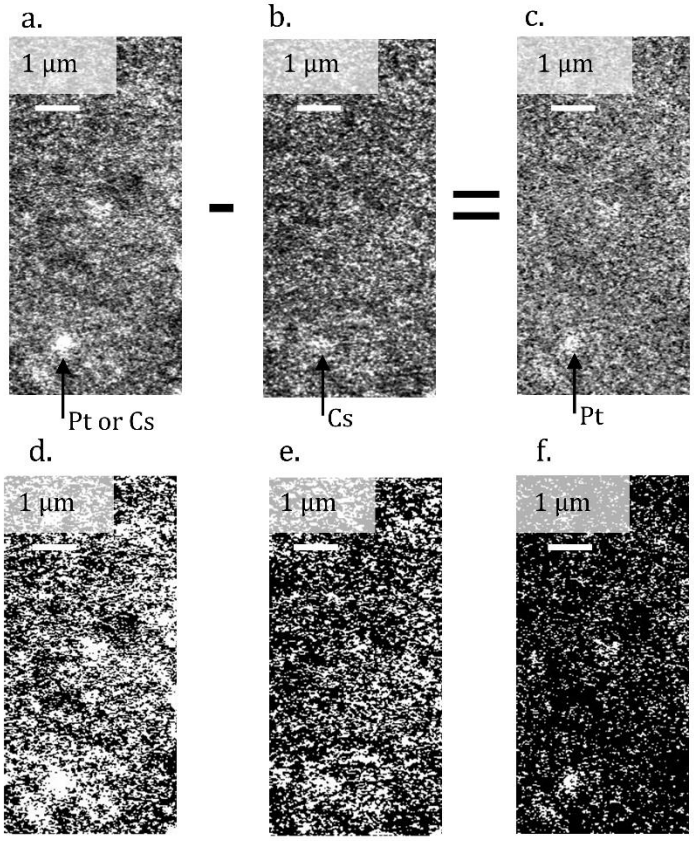

Figure 4-2. a) 11.7 keV image b) 11.5 keV image c) result of subtracting (b) from (a) d-f) thresholded images of respective scans. The bright spot in (a) could be either Pt or Cs. By subtracting (b) which Cs only, (c) shows Pt only.

This distinction is of critical importance as the distribution of Pt and Ionomer within a catalyst plays an important role in how the catalyst functions. The goal of imaging the material is to characterize this distribution using parameters like volume fraction, tortuosity, and size distribution. Table 4-1 shows that neglecting to separate Pt from

ionomer when performing these calculations results in overestimating the volume fraction and average size of the ionomer and underestimating the tortuosity factor.

Table 4-1. Properties of scans at the two energies. The combined Pt and Cs scan yields a significantly higher volume fraction and lower tortuosity than does the Cs only scan. The reported tortuosity is averaged across the three coordinate directions.

Scan	11.7 keV	11.5 keV
Visible Features	Platinum and Cesium	Cesium only
Volume Fraction Above Threshold	0.434	0.304
Average Tortuosity Factor	4.1	9.6
Average Size	115 nm	98.7 nm

Comparing the results in table 1 to the predictions in section 4.1, the volume fraction of Pt (13%) is significantly higher than the predicted (4%). The volume fraction of ionomer (30%) is lower than predicted (54%). This discrepancy is likely due, in large part, to the fact that the theoretical predictions do not take into account the fact that the electrode is hot-pressed. This process will compact the porous ionomer bound Carbon matrix, but

leave the Pt unchanged. This will cause the volume fraction of the ionomer and the Carbon to decrease and therefore that of the Pt will increase.

4.4.4 Finding for this material in particular

The low equivalent weight sample imaged here was found to have a uniform distribution of both Pt and Ionomer. Figure 4-3 shows a 3D volume rendering of the Pt (green) and Ionomer (blue) and the distribution of the two throughout the sample. This uniformity can be quantified by comparing the volume fraction of Pt or Ionomer for each cross section along an axis and finding the standard deviation of those values as shown in Fig S1. Averaging the standard deviations of the volume fractions of the three coordinate directions gives values of 0.02 and 0.04 for Pt and Ionomer respectively. These values are low compared to the respective volume fractions of 0.11 and 0.30, which indicates that

spatial variations in volume fraction are small. The platinum here is also in good contact with the ionomer, as shown in Figure 4-3d.

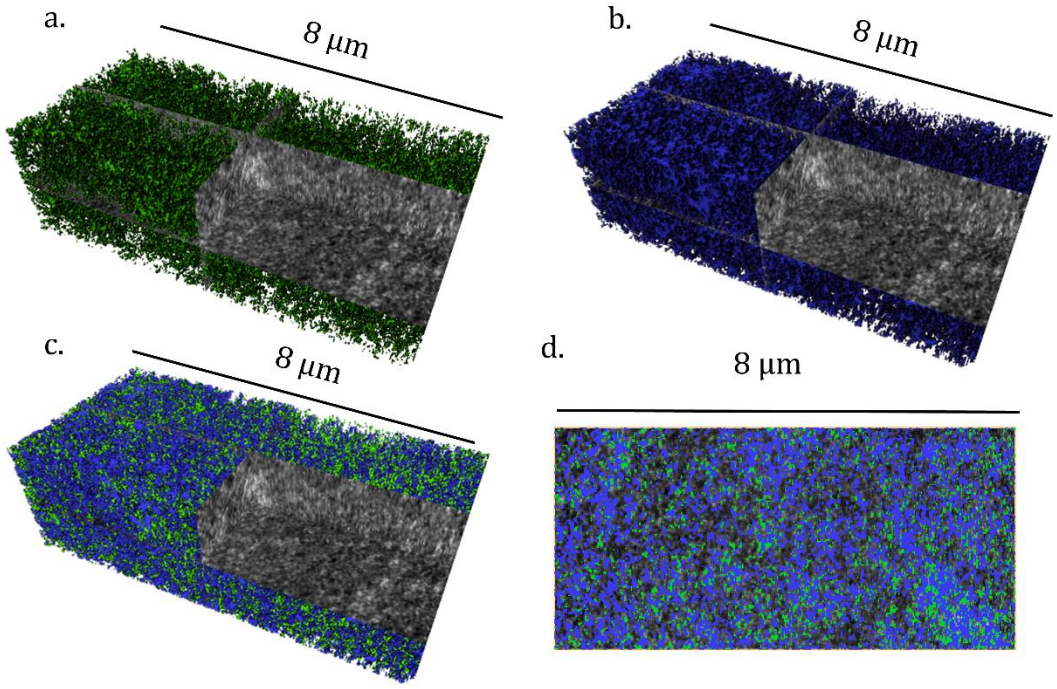

Figure 4-3. Volume renderings of a) Platinum b) Ionomer c) Platinum and Ionomer. d) Cross-section image with Pt (green) and Ionomer (blue) highlighted

XANES Chemical Mapping of NiCu Electrode

Another use of XANES is chemical mapping, as described in Chapter 2. Chemical mapping is useful for evaluating the chemical composition and distribution of platinum group metal (PGM) free electrodes. This study examines a nickel-copper electrocatalyst supported on Ketjen Black carbon (NiCu/KB). This catalyst is used in the anode of PGM-free electrodes, and the local distribution of Ni and Cu critical to its operation. XANES chemical mapping over an energy range from 8.3 to 8.5 keV was chosen to take

advantage of the nickel (Ni) K-edge located at 8.33 keV [27]. The results of this study are shown in Figure 4-4.

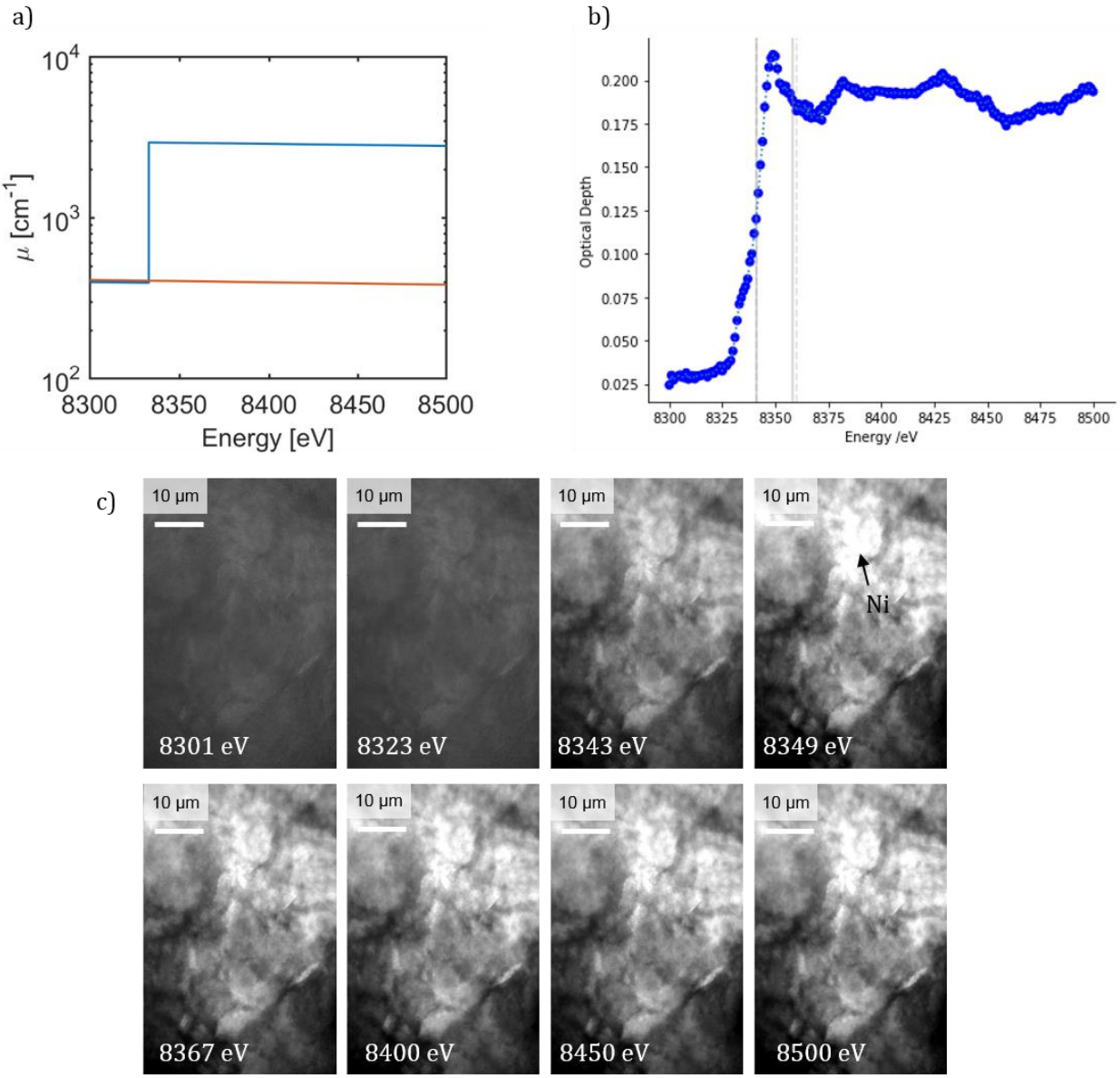

Figure 4-4. a) Ni (blue) and Cu (red) attenuation coefficients b) optical depth as a function of photon energy for a NiCu sample c) radiographs at various energies

The spike in attenuation (quantified using the optical depth) seen at the Ni K-edge confirms the strong presence of Ni in the sample. Below this edge, Ni and Cu have nearly

identical attenuation coefficients. The radiographs in Figure 4-4c show the distribution of the Ni within the sample.

4.5 *Chapter Conclusion*

The XANES two energy method for imaging ionomer distribution in Pt catalyst electrodes presented here provides the first definitive way to separate Pt from Cs stained ionomer in imaging analysis. This enables one to quantify several important properties of the ionomer—such as the volume fraction, tortuosity, and distribution—more accurately than with previous methods. It also makes it possible to determine if the Pt in the electrode is being used efficiently as it shows whether the Pt agglomerates are in contact with the ionomer. The XANES chemical mapping of a PGM-free NiCu/KB catalyst electrode shows the power of chemical mapping for identifying the constituent materials in a material and their distribution.

5 Micro CT *Operando*

5.1 *Chapter Introduction*

One of the biggest draws of hydrogen fuel cells as a replacement for internal combustion engines in automotive applications is the fact that their only physical by-product at the point of reaction is water. Water is produced in the cathode when the protons and electrons combine with oxygen (5.1).

$$O_2 + 4H^+ + 4e^- \rightarrow 2H_2O \tag{5.2}$$

The amount of water being produced is proportional to the current density by Faraday's law of electrolysis (5.2) [50].

$$MolH_2O = \frac{A}{2F}\int i \, dt \tag{5.3}$$

Where *Mol* is the number of moles produces, *A* is the active area of the cell, *F* is Faraday's constant, and *i* is the current density. One problem with this water production is that it can clog the pores of the porous catalyst layer or gas diffusion layer (GDL), a condition known as flooding [4, 51]. Eller et al. developed an *operando* fuel cell to visualize the water distribution in the GDL [8], as described in Chapter 1. This cell served as the inspiration for the cell presented here.

5.2 *Design*

5.2.1 Material selection

The most important quality of the cell is that it must be x-ray transparent. As x-rays pass through a medium, they are attenuated as described by the Beer-Lambert law (5.3).

$$I / I_0 = exp(-\mu l) \tag{5.4}$$

Where I_0 and I are the incident and resultant intensity of the x-rays, μ is the attenuation coefficient, and l is the thickness of the medium. A detailed derivation of the Beer-Lambert law may be found in Chapter 2. The attenuation coefficient is a strong function of the photon energy of the x-rays. Figure 5-1 shows the fraction of the intensity that is attenuated by a ¼ inch plate of Aluminum, gold sputtered PEEK, and Graphite over a typical micro CT energy range of 20-30 keV.

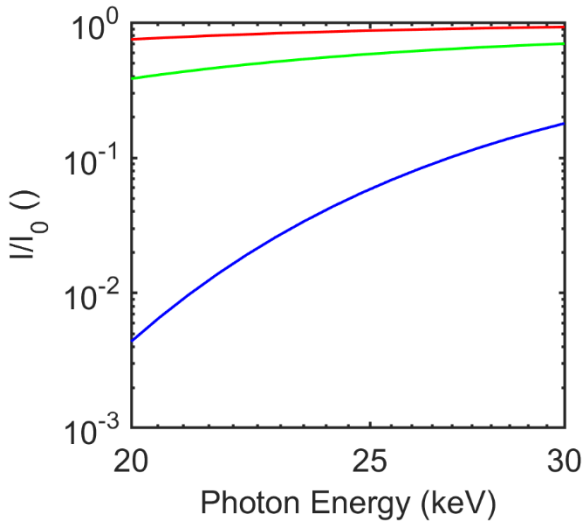

Figure 5-1. Attenuation of ¼ inch (0.635 cm) plates of Aluminum (blue), Graphite (red), and PEEK with 300 nm of sputtered Gold (green) as a function of photon energy over a typical micro CT range

Aluminum is completely opaque at these energies, however both graphite and gold sputtered PEEK offer good transparency. The rest of the parameters for material selection are summarized in Table 5-1.

Table 5-1. Parameters for material selection

	¼" 6061-T6 Aluminum	300 nm Gold Sputtered on ¼" PEEK	¼" Fuel Cell Grade Graphite
I/I_0 at 22 keV	0.014	0.47	0.80
Electrical resistance of 1cm X 4cm X thickness cuboid	2.5E-5 Ω	> 0.77 Ω	0.60 Ω

Thermal Conductivity	167 W/mK	0.273 W/mK	275 W/mK in plane 5.0 W/mK thru plane
Max displacement of 1cm X 4cm X ¼" cuboid under 6 kN of force	0.27 mm	4.8 mm	1.9 mm
Durability	Excellent	Gold sputtering is prone to being scraped off	Brittle – will break if dropped or over compressed
Machinability	Most Difficult	Medium difficulty	Easily machined with desktop CNC router

The electrical conductivity is based on a 1cm X 4cm cuboid that is 0.635 cm thick for the aluminum and graphite samples and 300 nm thick for the gold. This demonstrates that while gold has a very high electrical conductivity, the layer of gold is so thin that the resistance of the plate is quite high. The actual resistance of the gold sputtered plate is even higher than the calculated 0.77 Ω because over time, the gold flakes off.

The maximum displacement is based on modeling the same 1 X 4 X 0.6 cm cuboid as in the electrical calculations as a simply supported beam using equation (5.4) [52]. The reaction forces were calculated by assuming that a #8-32 screw tightened to 5 Nm is attached to either end of the beam. This produces a force of 6 kN by equation (5.5), the

reaction to which is assumed to be distributed along the entire length of the beam as shown in Figure 5-2.

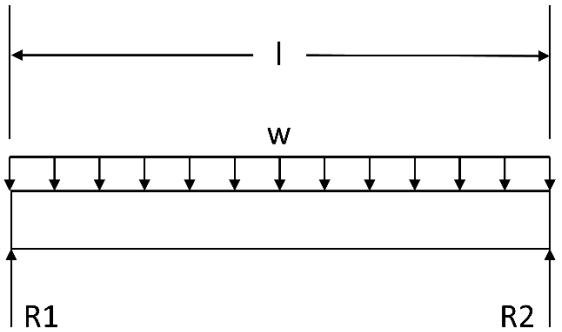

Figure 5-2. Simple supports uniform load

$$y_{\max} = -\frac{5wl^4}{384EI} \tag{5.5}$$

$$T = KF_i d \tag{5.6}$$

Where y_{max} is the maximum displacement, w is the distributed load in Nm^{-2}, l is the length of the beam, E is the Young's modulus, I is the moment of the beam, T is the torque of the bolt, K is the torque coefficient, Fi is the bolt preload, and d is the diameter of the bolt.

The final version of the micro CT cell sought to combine the most advantageous properties of both the Aluminum and the Graphite. It consists of graphite plates supported by an aluminum backing along the entire length of the cell, except for the region that is left open to allow x-rays to pass through as shown in Figure 5-3.

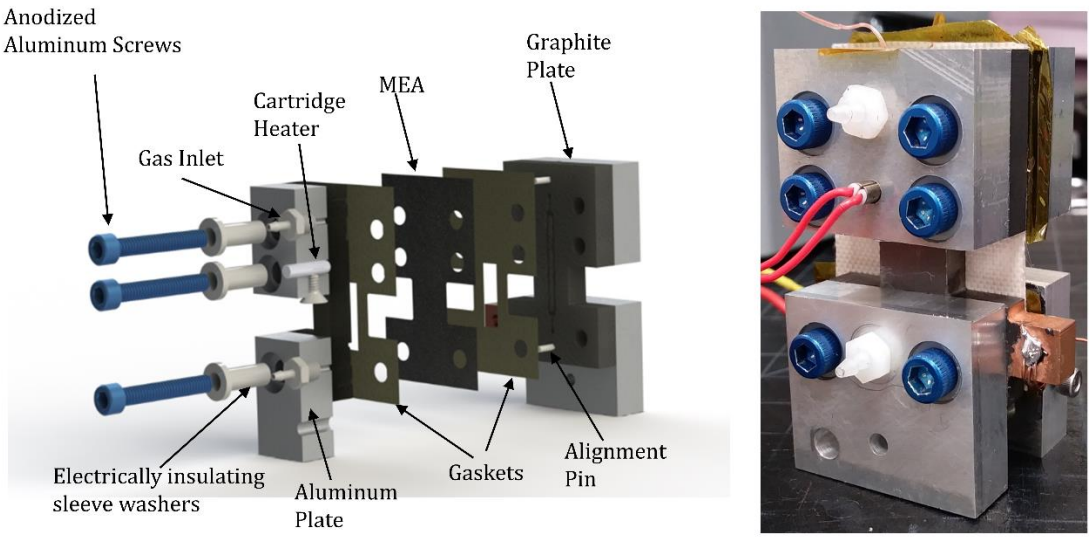

Figure 5-3. Micro CT Operando Cell

This design allowed the aluminum plates to provide all of the mechanical compression, as shown in Figure 5-4b. Uniform and strong mechanical compression are important for good fuel cell performance [53]. Typically, incompressible Teflon gaskets are used to absorb the stress. The thickness of the gaskets is chosen in such a way that the overall porous media components within the fuel cell are compressed by 15 – 20 %. While the section that is not supported by the aluminum plates does not exhibit very good compression, it is a relatively small portion of the length of the channel. Furthermore, the strong compression on either side of the unsupported region do not allow it to bow out visibly as was the case in earlier designs Figure 5-4a. The compression pattern was measured with Fuji Prescale Low Film that registers a range of 2.5-10 MPa.

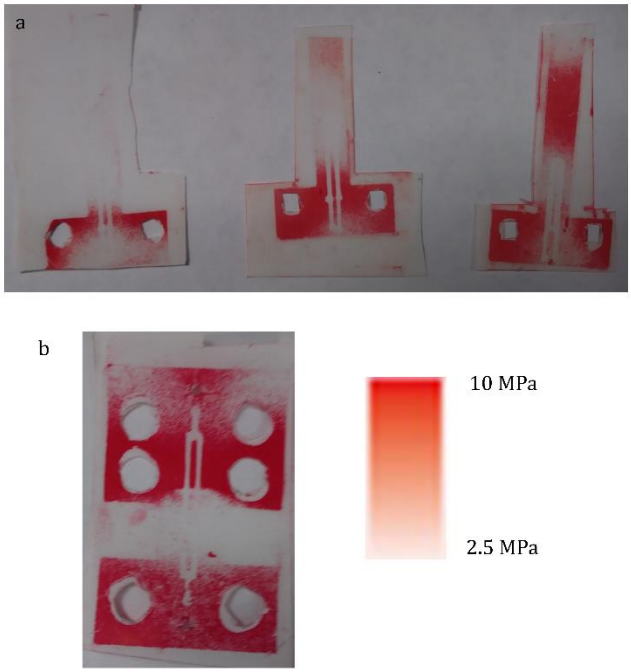

Figure 5-4. Compression pattern of Cell a) previous designs b) final design

5.2.2 Flow channels

The graphite plates can be easily replaced to allow different flow channel designs. The cell is also easy to assemble and disassemble, thus conserving valuable synchrotron time. The ability to use different flow channel designs allow this cell to be run as either a fuel cell or an electrolyzer. Serpentine channels are ideal for fuel cells, whereas parallel channels are optimal for electrolyzers [54]. In the case of fuel cells, humidified hydrogen gas is fed to the anode inlet, and humidified air is fed to the cathode inlet. As these gases flow along the length of the channel, they diffuse into the membrane and are consumed in the reaction. The by-product of this reaction, water, is produced on the cathode and exits the fuel cell through the cathode outlet. Because these diffusion reactions take place over the length of the channel, it is optimal to have a channel that is as long as possible, thus making serpentine channels optimal. Figure 5-5 shows the fuel cell and electrolyzer channel designs.

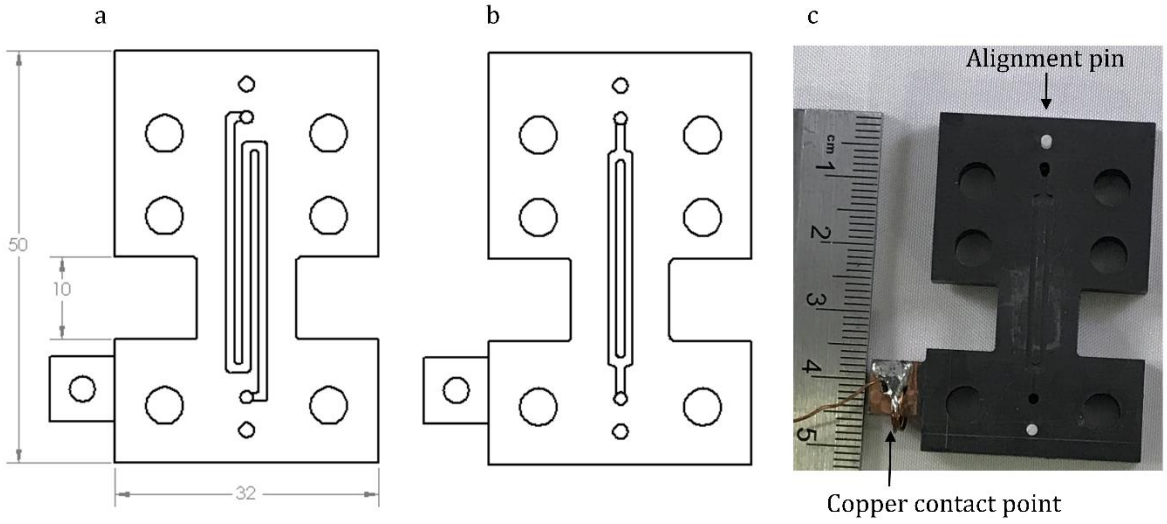

Figure 5-5. Fuel Cell and Electrolyzer flow channel designs. Marked dimensions are in millimeters and all channels are 1mm wide X 1mm deep with 1mm land. A) Fuel Cell serpentine channel design b) electrolyzer parallel channel design c) photo of electrolyzer design. The white alignment pins at the top and bottom of the channel ensures that the anode and cathode channels are in precise alignment. The Copper electrical contact point reduces contact resistance between the plate and the wire

Two factors influenced the choice of channel dimensions. Firstly, the channel and land must all fit within the 3 mm field of view of most micro CT setups. Secondly, the flow of fluids through the channel – humidified gases in the case of fuel cells and water in the case of the electrolyzer – should remain well within the laminar regime. The Reynolds number for the flow of humidified air through the channels at the typical rate of 0.25 slpm is 0.28, and that of water at 1 mL/min is 0.03 by equation (5.6). These Reynolds numbers place the flow at the low end of the laminar regime. The choice of 1 mm for the channel width was also based in part on the Dual Area Liquid Fuel Cell Fixture from Scribner Associates that also has 1 mm channels.

$$Re_d = \frac{QD_h}{\nu A} \tag{5.7}$$

One problem that early designs of the micro CT faced was that the channels on the anode and cathode side did not line up precisely. This was especially evident in the micro CT images where the offset could be seen clearly as shown in Figure 5-6a. The addition of alignment pins shown in Figure 5-3a and Figure 5-5c solved this problem, as seen in Figure 5-6b. 1/16" Acetal pins were chosen due to their low cost, tight diameter tolerance of ±0.127 mm, heat resistance to 104 °C, and electrical insulation. The temperature limit exceeds the maximum operating temperature of the cell, 60 °C, and the diameter tolerance allowed for the use of a press fit fastening between the pin and the graphite plate on the anode side. On the cathode side, a 0.191 mm clearance was used to allow for easy cell assembly while maintaining a precise alignment of the two plates. The use of a CNC milling machine with 0.076 mm accuracy (Rolland MDX or Bantam Tools) for the milling of the graphite plates ensured that the alignment pin holes were consistently placed relative to the flow channels.

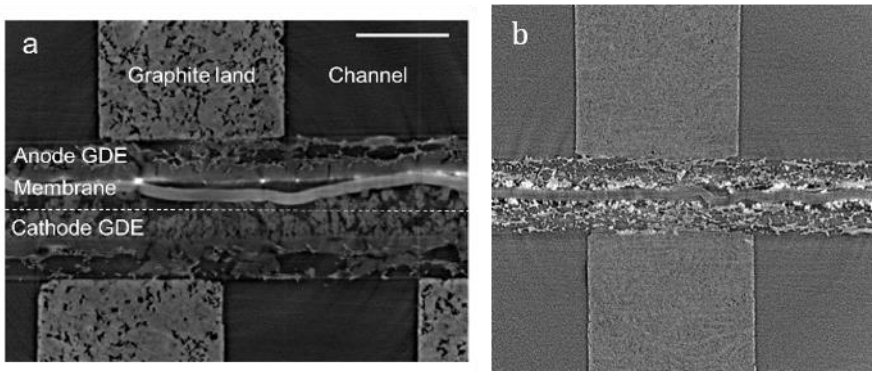

Figure 5-6. Micro CT cell images a) without alignment pins b) with alignment pins

5.2.3 Electrical and Thermal

Hydrogen fuel cells have a thermodynamic potential limit of 1.23 V. At these low voltages, any electrical resistance in the cell itself can significantly degrade the performance. Early designs of the micro CT cell suffered from high electrical contact resistance between the graphite plate and the copper wire that connected it to the potentiostat. This issue is complicated by the fact that the wire moves as the cell is rotated on the beamline stage. The most effective way to electrically join two components is soldering. Capelato [55] showed that while it is not possible to solder directly to the graphite, it is possible to electrodeposit copper to the graphite and then solder to the copper. This method reduced the electrical resistance between the wire and the graphite plate to 0.7 Ω from 1.8 Ω. While this method did significantly improve electrical conductivity, it did not provide the necessary mechanical strength as pulling on the wire could rip the copper off the graphite. While a significant amount of force was required to accomplish this, a stronger mechanical connection provides a better factor of safety. This was accomplished by wrapping the wire through a hole in the graphite to provide mechanical security, then soldering that wire to the copper contact to provide electrical conductivity as shown in Figure 5-5c.

The operating temperature of most fuel cells is between 60 and 80 °C [56] . In the case of this cell, the operating temperature was 60 °C. This was accomplished with a 0.75 W cartridge heater inserted into the aluminum plate on both sides of the cell as shown in Figure 5-3. Each side also had a thermocouple inserted between the aluminum plate and the graphite plate which enabled feedback control. An Arduino Uno microcontroller running a proportional-integral-derivative (PID) loop controlled a pair of transistors which provided a 5V pulse width modulation (PWM) signal to the heaters. The

proportional, integral, and derivative gains of the PID controller were 1, 10, and 3 respectively. Figure 5-7 shows the step response of the heater system. A more powerful heater would be able to reach the steady state temperature more quickly.

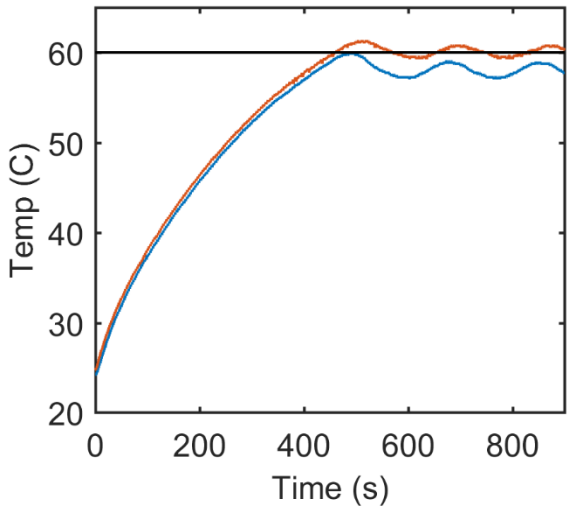

Figure 5-7. Step response of Anode heater (blue) and Cathode heater (red)

For optimal performance, the temperature distribution along the length of the channel should be as uniform as possible. Graphite is an ideal material for this as its high in-plane and low through-plane thermal conductivity make it a very good heat spreader. Modeling the cell as a 5 cm 60 °C vertical plate in quiescent 20 °C air gives a heat transfer coefficient due to natural convection of 7.3 $Wm^{-2}K^{-1}$ by (5.9)[57].

$$Nu = 0.680 + \frac{0.670 * Ra^{1/4}}{[1 + (0.429/Pr)^{9/16}]^{4/9}} \tag{5.8}$$

$$Ra_L = Gr_L Pr = \frac{g\beta(T_s - T_\infty)L^3}{\nu^2} Pr \tag{5.9}$$

$$Nu = \frac{hL}{k} \tag{5.10}$$

Where h is the heat transfer coefficient, k is the thermal conductivity of the fluid, Nu is the Nusselt number, Ra is the Rayleigh number, Pr is the Prandtl number, g is the

acceleration of gravity, β is the volumetric thermal expansion coefficient, T_s is the surface temperature, T_∞ is the bulk temperature, L is the length of the plate and ν is the kinematic viscosity. This convection coefficient was then used to perform a thermal analysis of the micro CT cell using SolidWorks Simulation Toolbox. Since the cell is symmetric about the plane of the MEA (Figure 5-3), that plane can be modeled as an adiabat. This allows the cell to be modelled using one graphite plate with an adiabatic boundary condition on the channel side as shown in Figure 5-8. For simplicity, the aluminum screws were neglected from the model. The PID controlled heater can be modeled as an area of constant temperature at the location where it contacts the graphite plate.

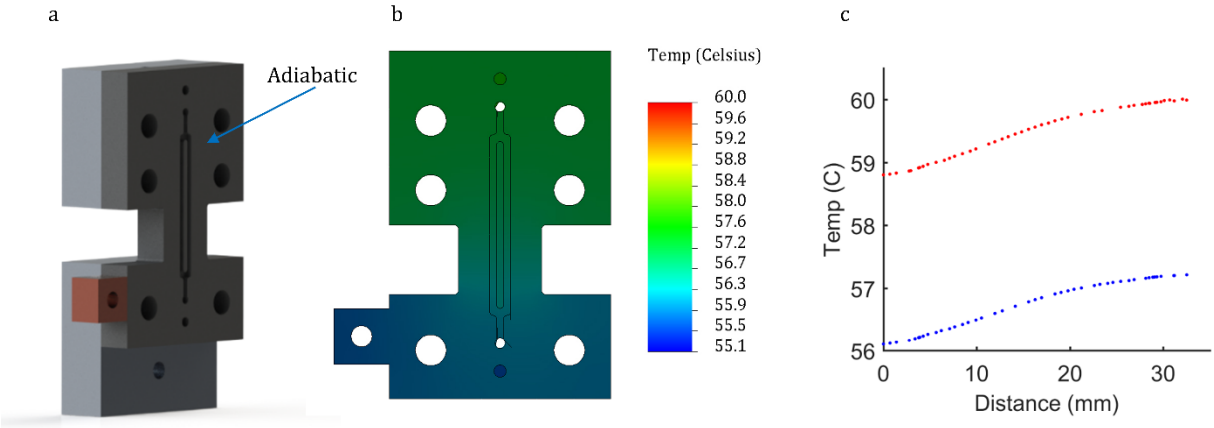

Figure 5-8. a) Model for thermal analysis – the channel face is modeled as adiabatic, all other faces are modeled as having a convective heat transfer coefficient of 7.3 $Wm^{-2}K^{-1}$ b) Temperature distribution along graphite plate c) Temperature distribution along the length of the channel when the heater is set to 60 °C (blue) and 63 °C (red)

The thermal analysis shows that the temperature varies only 1.1 °C along the length of the channel. It also shows that in order to maintain the channel at 60 °C, the temperature of the heater should be set to 63 °C in order to account for the heat lost to the surroundings.

5.3 *Discussion/Results*

Since water attenuates x-rays weakly, studies that aim to show water content in carbon materials should theoretically be imaged in phase contrast. However, phase contrast can introduce artefacts from the sample holder. The images were therefore taken in absorption contrast mode, using image subtraction to see the water clearly. This method of water separation was first developed by Eller et al. [8]. The first scan is taken with the cell at open circuit voltage (OCV) conditions, which will not produce any water by Faraday's law of electrolysis (5.3). Since the gases are humidified to 100% RH before flowing into the cell, they will cause the MEA to swell. This is necessary so that it will be possible to align the dry and wet images. The second is taken with the cell running at a specified current density. The reason the cell is maintained at constant current, and not constant voltage is that the amount of water produced is proportional to the current density by Faraday's law of electrolysis (5.3). After some time, the cell will reach steady state where the rate of water production and removal will be equal. It is at this time when the scan is taken to see the steady-state water content in the GDLs, channels and if possible in the catalyst layer. This procedure is often repeated for several different current densities in order to establish a trend in water content. The dry image is then subtracted from the wet image in order to see the water. This process can be done in absorption contrast mode, as the minute changes in attenuation from the water will be visible once

the images are subtracted. This process is shown in Figure 5-9. It is important that the reference scan be at the same relative humidity (RH) as the one with current density. This is because Nafion membrane swells when humidified, so image alignment and subtraction will not be possible for images taken at different RHs.

For this study, a PGM-free cathode that is based on a Fe-N-C catalyst was selected. Due to electrode's large thickness, as Fe-N-C is not as active as Pt, a larger loading of 4 mg/cm^2 was needed. The catalyst was deposition onto the GDL, forming gas diffusion electrode (GDE) and pressed against the membrane. Pt-based catalysts are typically an order of magnitude thinner, and thus the water distribution in them cannot be resolved using micro CT. The thickness of the PGM-free catalyst allows the water distribution to be probed in micro CT. The anode GDE was made of Pt electrocatalyst.

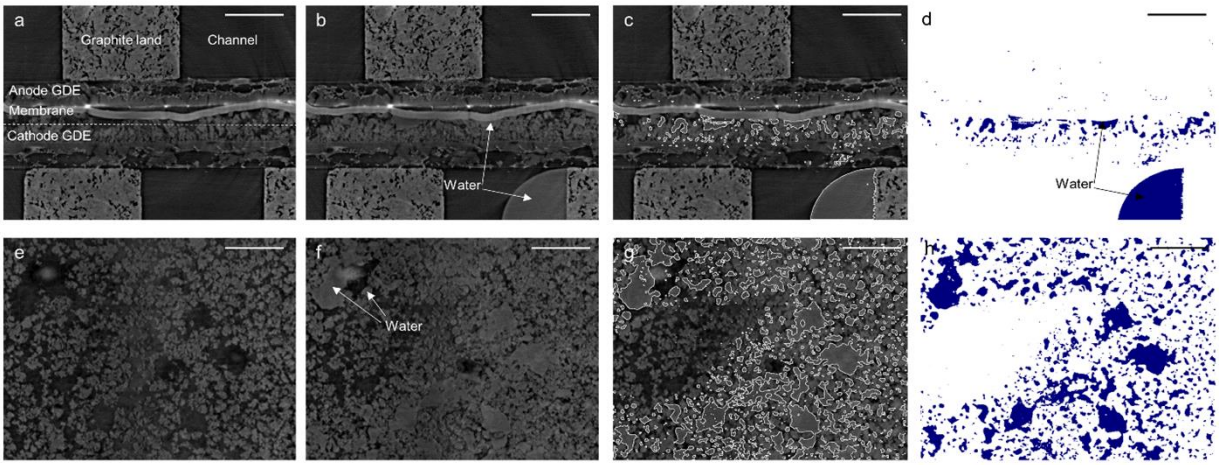

Figure 5-9. Micro CT operando images of a PGM-free fuel cell a) dry image b) wet image c) wet image with water highlighted d) water only e-h) through plane versions of (a-d)

This imaging shows that the water forms predominantly in the cathode GDE and channel. This agrees with the theoretical prediction, as the cathode half reaction (5.10) is the one with water as a product.

$$O_2 + 4H^+ + 4e^- \rightarrow 2H_2O \tag{5.11}$$

Closer inspection reveals that the water forms primarily at the interface between the catalyst layer and the membrane. The use of a GDE decreases the gap between the GDL and the catalyst, but increases the gap between the catalyst and the membrane. The large voids observed at the GDE|membrane interface are due to inhomogeneous evaporative drying of deposited ink onto the GDL. These voids can be seen on the cathode side of the membrane-GDE interface in Figure 5-9a and the large water agglomerates that formed there are in Figure 5-9b-d. The water formed in the cathode CL can be removed either directly into the cathode channel (through the cathode GDL) or across the membrane to the anode channel. The lack of visible water on the anode side indicates that the former removal method is the dominant one. This experiment was conducted with the cell kept at a constant 30°C temperature, which means that there were not any significant thermal gradients through the thickness of the cell due to the low heat of reaction. Therefore, phase-change induced flow and local condensation under the lands are negligible.

This experiment was conducted with an earlier version of the micro CT cell, which was not capable of the levels of compression that the current cell is. This experiment was repeated with the newer cell and the voids at the GDE|membrane interface were still present, which confirms the earlier hypothesis that they are due to the inhomogeneous evaporative drying process, and not a lack of compression.

5.4 *Chapter Conclusion*

The micro CT fuel cell presented here offers significant advantages over the prior state of the art *operando* cells. Over the iterations of its design, mechanical compression, electrical conductivity, and electrochemical performance have significantly improved. The images taken with this cell have clearly shown where in the fuel cell liquid water has a tendency to pool. This same procedure can be repeated for different catalyst layers and GDLs to evaluate their water removal performance. This cell can also be run as an electrolyzer to track the rate and evolution of the oxidation reaction.

6 Nano CT *Operando*

6.1 *Chapter Introduction*

While micro CT is useful for visualizing water in large features, smaller features require the high resolution of nano CT. Particularly, water distribution in the catalyst layer that is 10 um thick should be probed with nano CT method, as micro CT will resolve only 9 points along the thickness of the catalyst layer. Presented here is the first ever fuel cell developed for *operando* nano CT study. All of the same considerations described in the previous chapter apply here as well, with the addition of some new challenges that exist only for nano-scale study due to lower energies of photons and smaller imaging field of view.

6.2 *Design*

6.2.1 Material selection

The nano CT cell presents several challenges not present in the micro CT. The first iteration of the micro CT was designed for use at 32-ID-C at the Advanced Photon Source (APS) at Argonne National Lab. This beamline cannot vary the energy for nano-

scale x-ray imaging with phase contrast and was set at 8 keV. As was the case for designing the micro CT cell, the Beer-Lambert law (6.1) can be used to determine which materials will be transparent enough for use in the nano CT cell.

$$I / I_0 = exp(-\mu l) \tag{6.1}$$

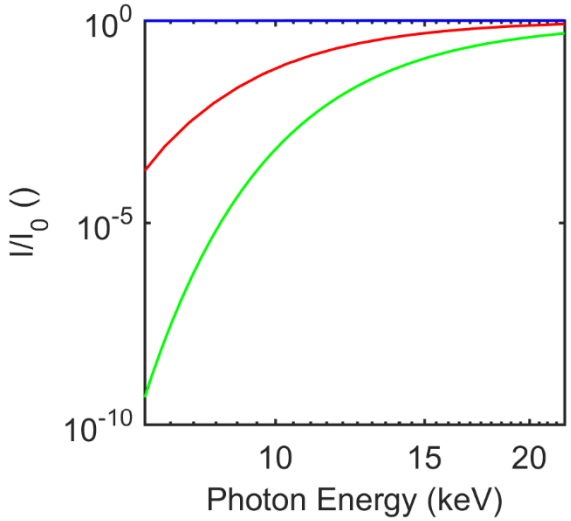

Figure 6-1. Attenuation of ¼ inch Graphite plate (red), ¼ inch PEEK plate (green), 15 µm Kapton window (blue) over a typical nano CT range

Figure 6-1 shows that a thin Kapton window is the only viable option at 8 keV. This poses a significant challenge for the design of the cell, as Kapton lacks the structural rigidity necessary to stay in place unsupported, let alone provide any compression to the MEA. This means that another material must be used for mechanical support of the cell. At 8 keV, there are no materials that can accomplish this that are also x-ray transparent. As the cell rotates on the stage, any structural members that are in the way of the beam will block the x-rays at certain angles as shown in Figure 6-2. It is therefore necessary to minimize the number of these missing angles through clever design.

6.2.2 Cell Geometry

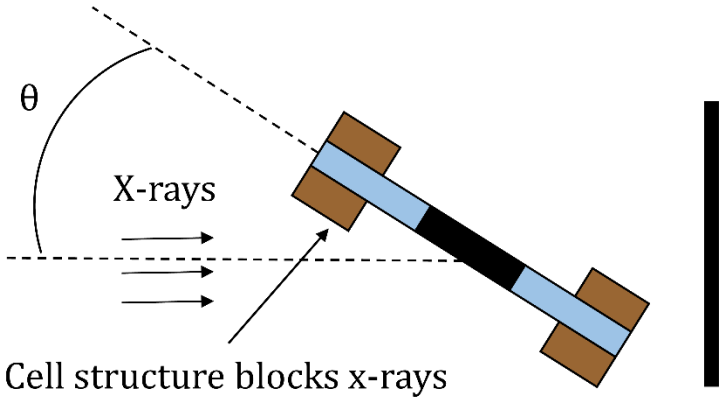

Figure 6-2. Top view of nano CT cell where θ is the angle of the cell relative to the beam. The cell structure blocks x-rays from reaching the collector when θ < 16°

In order to minimize the number of missing angles, the supports indicated by the arrow should be as narrow as possible while still maintaining structural rigidity. The original design called for these supports to be 2mm X 1mm. The 1mm dimension was then reduced to 0.75 mm by filing away some of the material. This decreased the size of the missing region by 1-2°. Additionally, the optics surrounding the sample mounting stage at the synchrotron impose a tight spatial constraint. The magnetic stage attachment on which the cell can be mounted is just 25 mm X 25 mm.

The necessity to use Kapton windows disallows traditional flow channels. Since the field of view of the nano CT beamline is just 80 μm, it is preferable to have a small electrochemically active area so that the current is concentrated within the field of view. Because of the small area and the need for Kapton windows, the best way to flow the gases to the membrane electrode assembly (MEA) is to have an open chamber into which gasses are flowed and from which they can diffuse into the MEA as shown in Figure 6-3.

In order to maximize the current density within the field of view, the MEA is cut in a T-shape and surrounded by Kapton to form a seal.

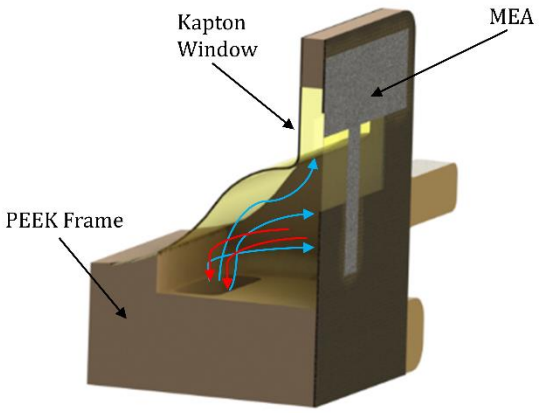

Figure 6-3. Flow Chamber – Blue arrows indicate gas supply, Red arrows indicate gas return

In order to flow gases into and out of the flow chamber, a specially designed base directs them from the supply tubes as shown in Figure 6-4a. The hydrogen gas has inlet and outlet tubes, however the air has only an inlet tube as shown in Figure 6-4b. The air outlet vents directly to the surroundings as it is not necessary to have a dedicated air extraction line. The rubber gasket prevents any gases from leaking between the base and the flow chamber.

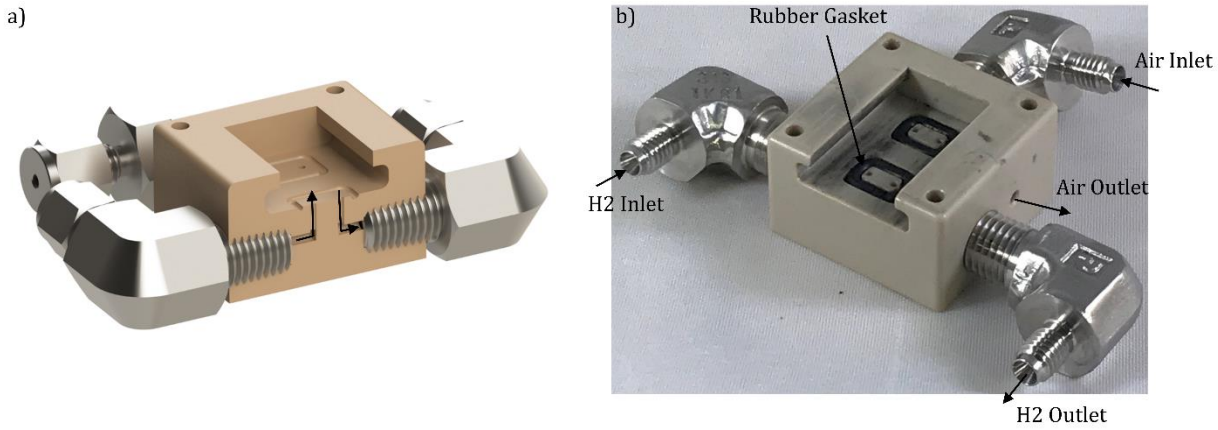

Figure 6-4. Nano CT cell base a) cutaway view with flow channels highlighted b) photo

The flow chambers slide onto the base as shown in Figure 6-5. Conventional fuel cell MEAs consist of a catalyst coated membrane (CCM) with a gas diffusion layer (GDL) on either side. Since the goal of this study is to quantify the water distribution in the catalyst layer of the CCM, it is necessary to cut windows in the GDL through which the CCM can be imaged without obstruction.

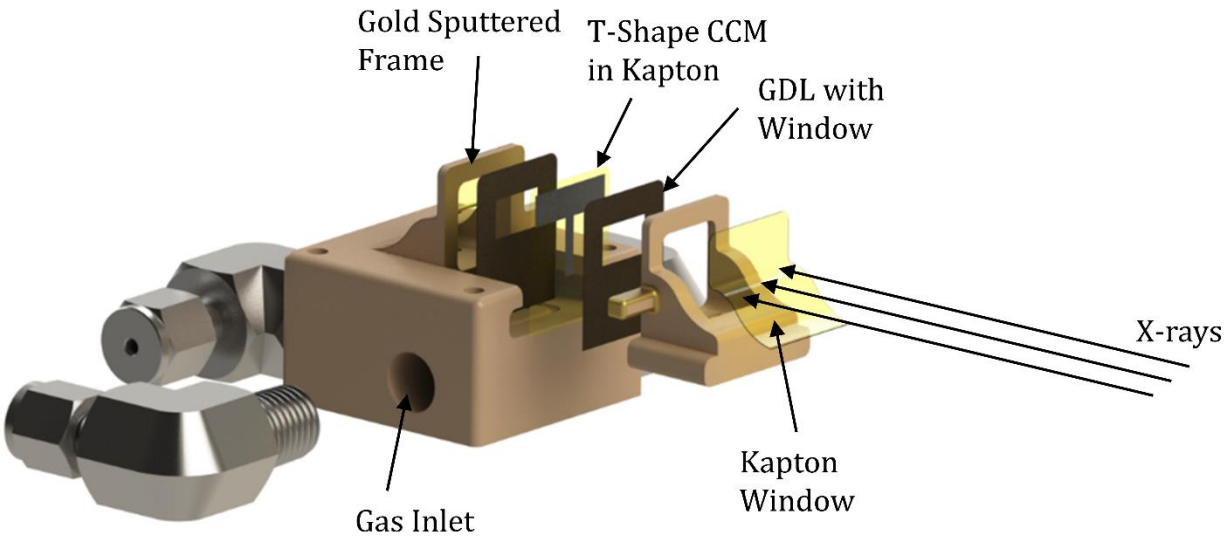

Figure 6-5. Exploded view of the assembled nano CT operando cell

The use of the GDL window enables the imaging of the CCM behind it, however it is also useful to image the GDL. Figure 6-6 shows a mosaic of five nano CT radiographs stitched together to form a single image with and without the window in the GDL. A radiograph is a single x-ray image taken without rotating the sample. When the GDL is present, the CCM cannot be seen behind it.

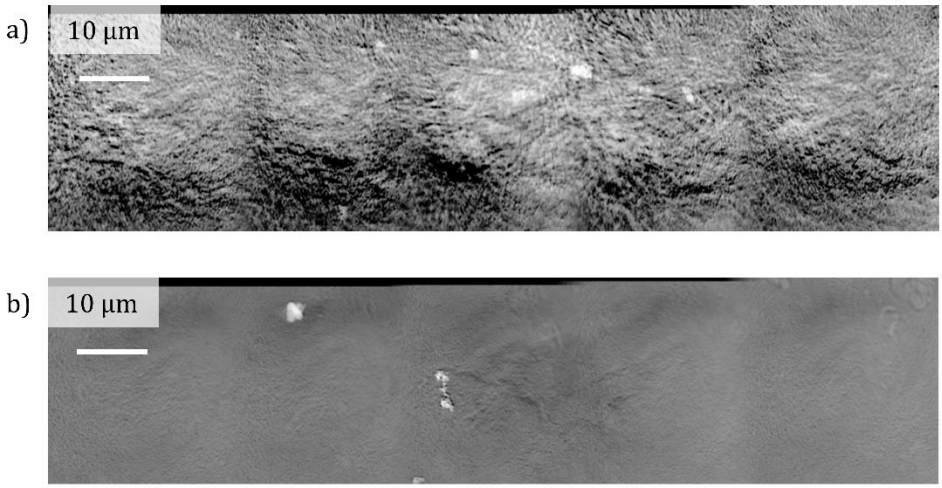

Figure 6-6. Mosaic of nano CT images a) without window in GDL b) with window in GDL

6.3 *Issues with First Generation Nano CT Cell*

6.3.1 MEA Movement

The first generation nano CT cell had several issues that limited both its performance and the ability to image it. The first was that the flow of gases into the flow chamber were causing the MEA to move slightly. Unfortunately, this motion was enough to blur the resulting nano-scale image. The solution was to add stability bars to the area below the field of view. Due to their complex geometry, the flow chambers are expensive to machine. The stability bars therefore had to be added to the existing part. This was accomplished by drilling small holes in the side of the chamber and threading a thin wire across the length. The wire was then epoxied in place and wrapped in Kapton tape so that it would be thick enough to come into contact with the MEA (Figure 6-7). The inlet of the flow chamber (the rectangular hole in Figure 6-3) was also covered with a scrap of GDL. This forced the incoming gases to diffuse through a porous membrane, as opposed to flowing directly into the cell, which dispersed the flow and prevented any one region from having a large velocity. The combination of these factors stabilized the MEA enough so that it could be successfully imaged.

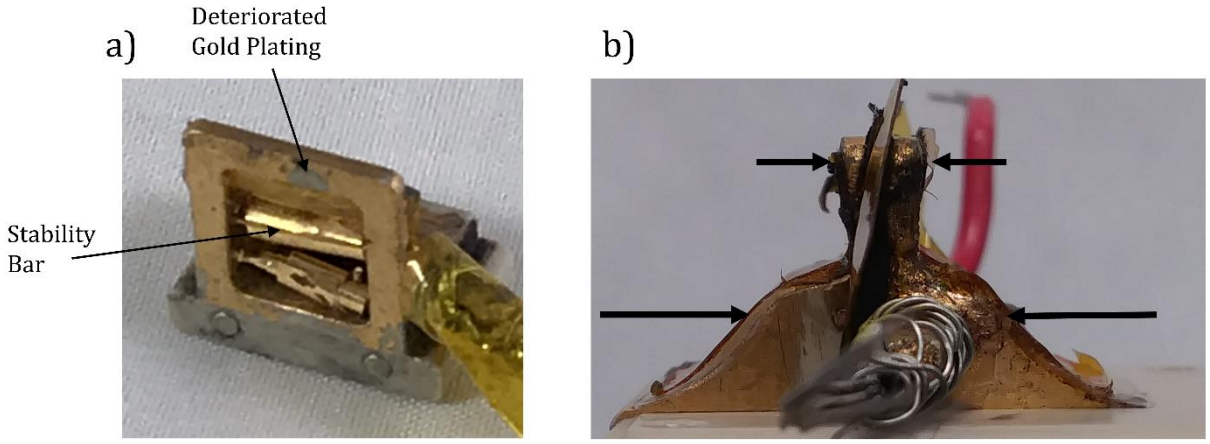

Figure 6-7. a) Flow chamber with added stability bars b) compression pattern

6.3.2 Electrical Conductivity

Another problem the cell faced was poor electrical conductivity. Figure 6-7a shows that the 300 nm of gold sputtering on top of the PEEK frame is quite fragile and can be flaked off easily. Furthermore, the fact that the gold was not annealed introduced inter-grain contact resistances within the deposited film. Additionally, there is no good way to electrically connect the gold sputtered frame to the copper wire that connects it to the potentiostat. Soldering is not an option, as it will not adhere to the gold. That leaves electrically conductive epoxy, which is mechanically weak. As the cell rotates on the stage, the epoxy is stressed and the bond risks breaking. When this happens, the electrical resistance between the wire and the frame spikes. Wrapping this joint in Kapton tape as shown in Figure 6-7a helps to secure it, however the risk of breakage is still high. The electrical resistance of the cell without an MEA and with fresh gold sputtering is 1Ω. After the cell has been used and the gold is flaking off and the epoxy connection has been fatigued, the resistance can reach the 10s or even 100s of Ω depending on the level of wear.

6.3.3 Mechanical Compression

The electrical conductivity issue is compounded by the lack of mechanical compression on the MEA. Fuel cells perform better under mechanical compression for a variety of reasons, among them is that the compression reduces electrical contact resistance [53]. The bottom sections of the flow chambers are held in place by the friction between them and the base as shown in Figure 6-7b. This provides an adequate amount of compression as indicated by the long arrows. The narrow supports in the upper part of the cell are too flexible to provide strong compression as indicated by the short arrows. Numerous attempts to compress the top of the cell above the imaging field of view have largely

failed due to the small area any clamping mechanism has to grip the cell and the fact that the gripping area is covered in slippery Kapton film, which makes it hard to grip. An integrated clamping mechanism is the best option to provide good compression, however it would require re-making the expensive flow chamber.

6.3.4 Beam Damage and Reconstructions

When x-raying a material, the energy of the attenuated x-rays described in the Beer-Lambert law (6.1) are absorbed into the material. The radiation dose absorbed is given by equation (1.2) [10].

$$R = \frac{NTE\mu}{\rho} \tag{6.2}$$

Where R is the radiation dose in keV/g (often converted to rad), N is the flux density in photons/cm^2/s, T is the exposure time in s, E is the photon energy in keV, μ is the linear attenuation coefficient in cm^{-1}, and ρ is the density in g/cm^3. If a material absorbs too much radiant energy, it will start to degrade. This can be seen in Figure 6-8, where 60 minutes of beam exposure reduced the thickness of the CCM by 66%. This figure was calculated by comparing two radiographs at the same angle. Radiographs are the raw x-ray projections used to reconstruct tomographs. Usually there are 720 radiographs (also called projections) spaced evenly between 0° and 180° of rotation with respect to the plane of the beam. It should be noted that the reconstruction algorithm inverts the color spectrum so highly attenuating features show up brightly. Radiographs do not perform this inversion, so highly attenuating features show up darkly. The reconstructed cross-section tomographs are shown as inserts in the radiograph images. In addition to the thinning visible in the x-ray images, the beam damaged the CCM enough to produce a crack that is visible to the naked eye.

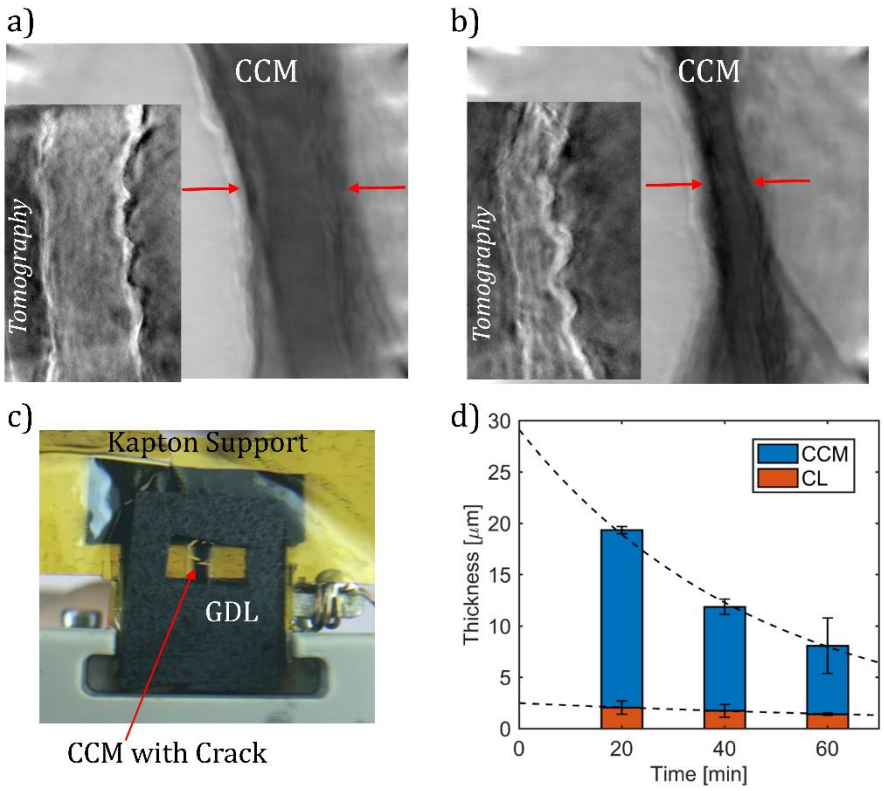

Figure 6-8. Beam damage to CCM a) sonogram and reconstructed tomogram of first scan after 20 minutes of beam exposure b) third scan after 60 minutes c) photo of MEA after scanning d) graph of CCM thinning due to beam damage

The effect of the missing angles described in Figure 6-2 can be seen clearly in Figure 6-8a and b. Due to the sides of the cell obstructing the beam, the 720 projections are spaced from 16° to 164° instead of the usual 0° to 180°. This results in the wavy lines that can be seen in the tomograms that are inset in each of the figures.

6.4 *Second Generation Cell – SSRL*

The first usable data taken with the nano CT cell was at beamline 6-2 at the Stanford Synchrotron Light Source (SSRL) at SLAC National Accelerator Laboratory. In order to avoid beam damage, the cell was imaged using radiography as opposed to tomography. This beamline does not have a phase ring, so all imaging was done using absorption

contrast. Radiography is a 2D imaging technique that exposes the sample to the beam for 1/720 the amount of time that tomography does as it only requires a single exposure. The major disadvantage is that it does not allow for 3D reconstruction. In order to expand the field of view, five scans were taken of each sample and stitched together to form one large image called a mosaic. Figure 6-9 shows the images that were taken, as well as the electrochemical performance of the cell. The first scan was taken with dry air flowing over the CCM in order to provide a dry baseline image. The cell was then fed humidified hydrogen and air. The second scan was under open circuit voltage (OCV) conditions. This is done by applying an infinite impedance across the cell so that no current flows. While no water is produced in this process, since water production is proportional to current by the Beer-Lambert law (6.1), there is still water reaching the CCM by condensation from the humidified gases. The cell was then imaged under three different current conditions by applying a specified voltage across the cell. The current response to these constant voltages are plotted in Figure 6-9b.

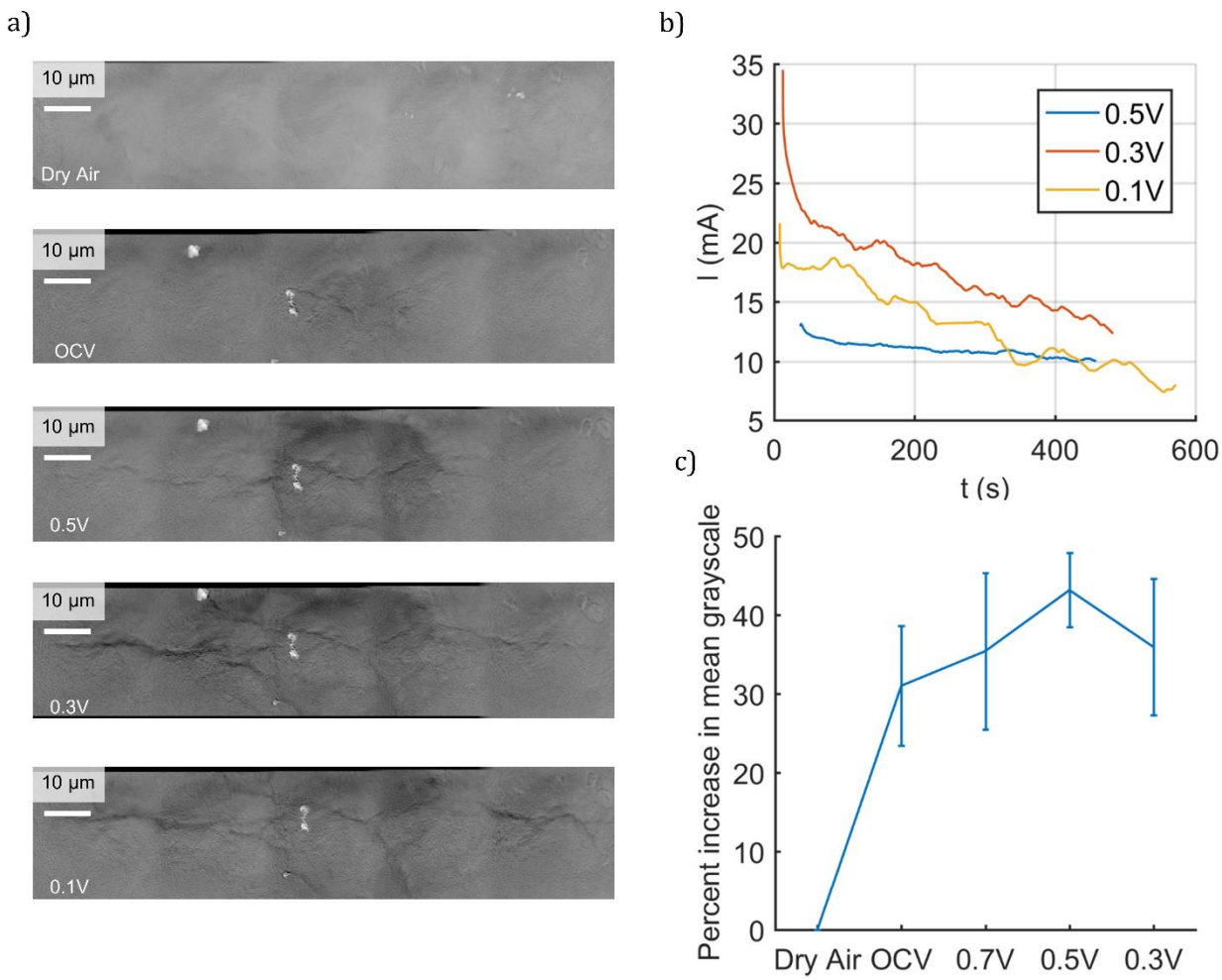

Figure 6-9. a) Radiographs of the nano CT cell CCM under progressively higher current conditions b) Current vs time curve for the 0.5, 0.3, and 0.1 V runs c) Percent increase in greyscale value (proportional to decrease in attenuation) of each image relative to the dry air image

6.4.1 Results

The fact that the current density is higher at 0.3V than at 0.1V shows that the cell may have a limit to the maximum current it can handle. The overall performance of the cell is highly inconsistent, due in large part to the lack of mechanical compression and poor electrical conductivity discussed earlier. The runs shown here represent the best case

scenario in terms of this cell's electrochemical performance. The window cut in the GDL also degrades the performance, as the GDL acts as an electrical conductor between the CCM and the frame of the cell.

The increased current density caused the formation of cracks that become more pronounced with increasing current density. It also caused the overall attenuation of the sample to decrease. This can be seen in Figure 6-9a since the reconstruction algorithm inverts the color contrast so highly attenuating objects appear more brightly. The very bright spots in Figure 6-9a are gold fiducials placed on the sample to help align the imaging equipment. The grayscale value of each pixel in the resultant image is proportional to the attenuation of the sample at that point, however the relationship between the intensity calculated using the Beer-lambert law (6.1) and the grayscale value is nonlinear due to the camera lens, the reconstruction algorithm, and the image processing software. The increase in grayscale value is plotted in Figure 6-9c. This trend of decreased attenuation is the opposite of the intuitive prediction, which states that water displaces air in the pores of the catalyst layer. Since the attenuation coefficient of water is higher than that of air (Table 6-1), the attenuation of the sample should increase with increased water content in the CCM. Instead, a trend of decreasing attenuation is seen. This could be due to the formation of cracks that can be seen in Figure 6-9a. As the crack spreads, the once uniform carbon and Nafion layer is bunched up to make way for pockets of water. Since water has a lower attenuation coefficient than either carbon or Nafion, this would decrease the attenuation. Due to the limited 2D nature of radiography, this hypothesis must be validated with 3D tomography data.

Table 6-1. Attenuation coefficients of CCM substances at 8 keV

Substance	Linear Attenuation Coefficient at 8 keV – μ (cm^{-1})
Carbon	9.66
Water	0.354
Air	8.89×10^{-3}
Nafion	15.0

The same procedure was then repeated for a cell without a window cut in the GDL. The addition of a complete GDL vastly improved the electrochemical performance of the cell in terms of both maximum current and the cell's ability to maintain a constant current for a prolonged period of time (Figure 6-10b). As discussed previously (Figure 6-6), the GDL completely blocks the view of the CCM behind it. This is due to the fact that the CCM is 30 μm thick, whereas the GDL is 225 μm thick. This means that the CCM will absorb about 4% of the incident intensity, whereas the GDL will absorb 20%, by the Beer-Lambert law (6.1). In the case of the GDL, there was no discernable trend in the grayscale value of the radiographs. This could be due to the porous nature of the GDL fibers causing the grayscale values to fluctuate. Another metric to quantify the water uptake in the GDL is to track the distance between features. If the distance between two features increases when water is introduced to the cell, the increase must be due to swelling. This can be seen in Figure 6-10a where the distance between two gold fiducials was tracked over all of the runs and graphed in Figure 6-10c. That distance increased significantly when water was first introduced to the GDL, then remained relatively

constant for the rest of the operation. This suggests that the maximum amount of water that can be held in the pores has been reached and additional water produced is being removed elsewhere. Differentiating Faraday's low of electrolysis (6.3) gives the rate at which water is being produced in moles per second.

$$\frac{dMolH_2O}{dt} = \frac{A}{2F} i \tag{6.3}$$

$$\frac{dMolH_2O}{dt} = \frac{I}{2F} \tag{6.4}$$

Where $MolH_2O$ is moles of water, A is the electrochemically active surface area, F is Faraday's constant, and i is the current density in amps/cm^2. Since the current density is current divided by area, it can cancel with the electrochemically active surface area to form (6.4) where I is the current. Using the 4 mA observed for the 0.7V run, water is being produced at 21 nmol/s.

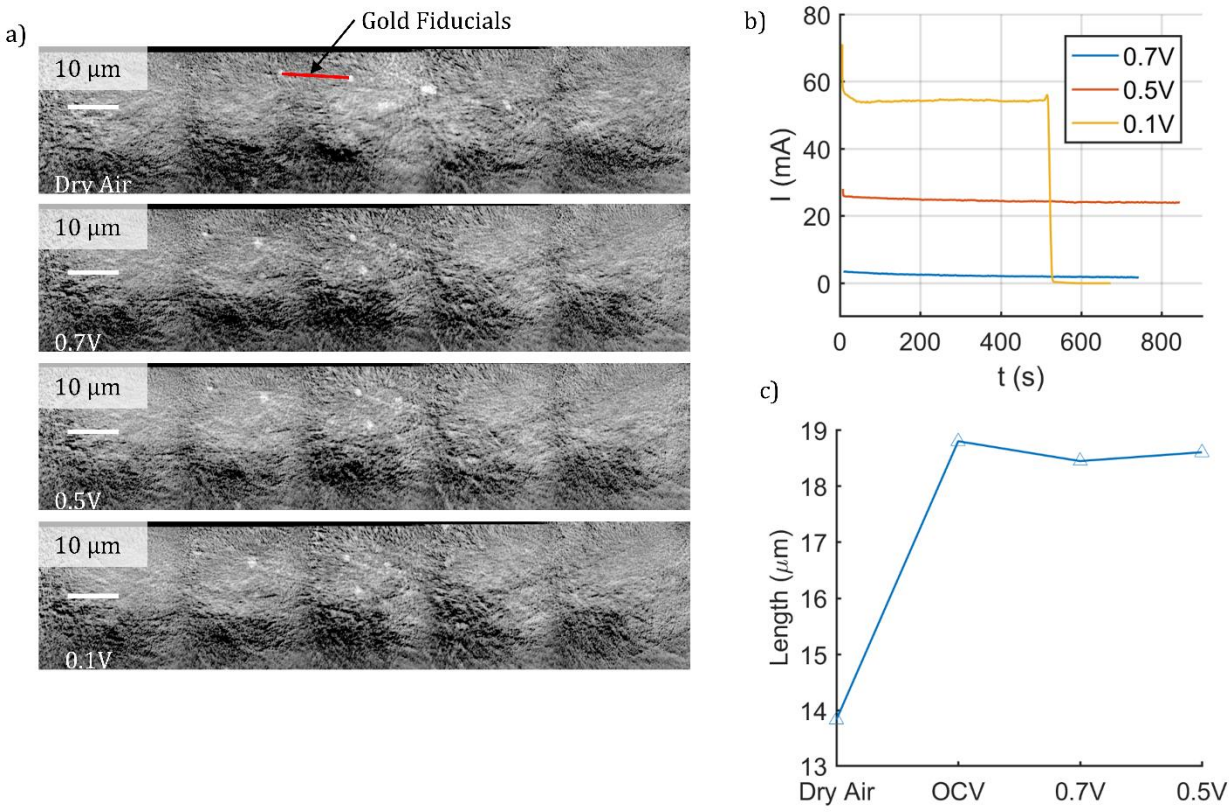

Figure 6-10. a) Radiographs of the nano CT cell GDL under progressively higher current conditions b) Current vs time curve for the 0.7, 0.5, and 0.1 V runs c) Swelling of the GDL as tracked by measuring the distance between the gold fiducials marked in (a)

6.5 *Third Generation Cell – ESRF*

The third generation cell was tested at beamline ID16B at the European Synchrotron Radiation Facility (ESRF) in Grenoble, France. This beamline is different from either of the previous beamlines in that it can perform nano CT analysis at 17.5 keV instead of the 8 keV at the other two beamlines. This puts it at the high end of typical nano CT energies and significantly changes the attenuation properties of the materials used to construct the cell as shown in Figure 6-1 and Table 6-2.

Table 6-2. Attenuation of materials at 8 keV and 17.5 keV

Material	8 keV I/I_0	17.5 keV I/I_0
1/4” Graphite (2 x 1/8” plates)	0.002	0.51
2 mm PEEK (2 x 1mm bars)	0.01	0.64
25 µm Kapton Film	0.97	0.99

This significantly improves the ability to image the cell, as the 1 x 2 mm PEEK frame that blocks the beam as shown in Figure 6-2 is now transparent enough to be imaged through. This will vastly improve the reconstruction quality as it will remove the wavy lines seen in Figure 6-8. Additionally, it is now possible to scan through the 1/8” graphite plate. This allows for the replacement of the flow chamber in Figure 6-3 with the graphite plate shown in Figure 6-11.

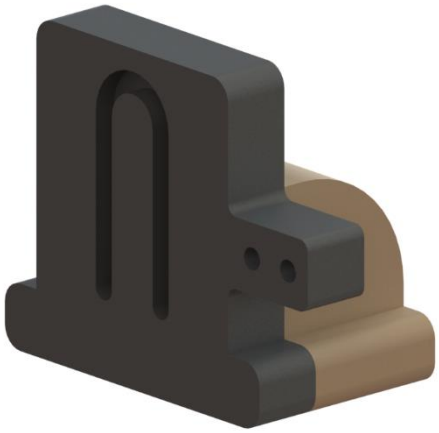

Figure 6-11. Nano CT cell graphite plate

This plate improves the performance of the cell by decreasing the electrical resistance and improving the compression. When the graphite plate cell was scanned at ESRF, the porous structure of the graphite plates produced phase artifacts that made the sample itself difficult

to see. A solution that offered a compromise between electrochemical performance and the ability to image the sample was to use a graphite plate on the cathode side and the flow chamber on the anode side. The use of only one graphite plate reduced the phase artifacts enough that the sample was visible. The graphite was used on the cathode side because the limiting factor in a hydrogen fuel cell is the sluggish oxygen reduction reaction (ORR) that takes place on the cathode side.

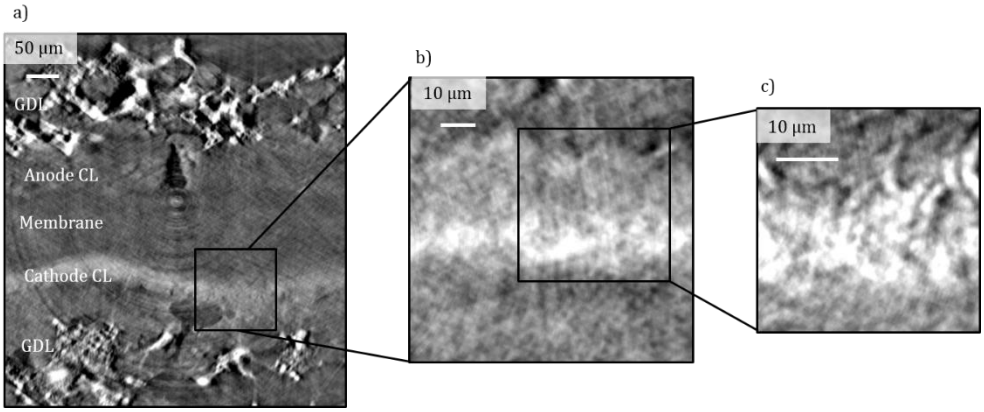

Figure 6-12. Operando cell at ESRF a) micro CT mode b) 100 nm c) 50 nm

ESRF beamline ID16B uses Kirkpatrick-Baez (K-B) mirrors to focus x-rays on the sample [58]. The advantage of this system is that by varying the distance from the sample to the detector, it is possible to change the resolution. This allows for multi-scale imaging at both micro- and nano-CT using identical location. For example, Figure 6-12a, micro CT resolution, shows the overall structure of the MEA but the finer details of the CL are missing. Figure 6-12b, with 100 nm resolution, shows the full catalyst layer, and Figure 6-12c shows even finer features of this layer. Furthermore, there is no evidence of significant beam damage, as the membrane's thickness has not changed.

6.6 *Fourth Generation Cell – Under Development*

The first generation nano CT cell was designed in the spring of 2016 and since then the advanced in both the micro CT and nano CT cells have highlighted its design flaws. An analysis of the positive and negative aspects of the nano CT cell design are summarized in Table 6-3.

Table 6-3. Nano CT cell design analysis

Advantages	Disadvantages
Modular – can use graphite plates or PEEK flow chambers	Poor electrical conductivity
Small size fits on nano CT stage	Poor mechanical compression
	Expensive to manufacture – base cost $700
	Gas inlets stuck out from side too far

Presented here is a generation 4 design for the nano CT cell that retains all of the advantages of the previous generations while addressing all of the disadvantages. Many of the improvements are based on lessons from the micro CT cell. This new cell uses graphite plates for all of the area of the cell that is outside the field of view of the beam which will greatly improve electrochemical performance. It also takes advantage of the electrodeposited copper solder connection used in the micro CT cell.

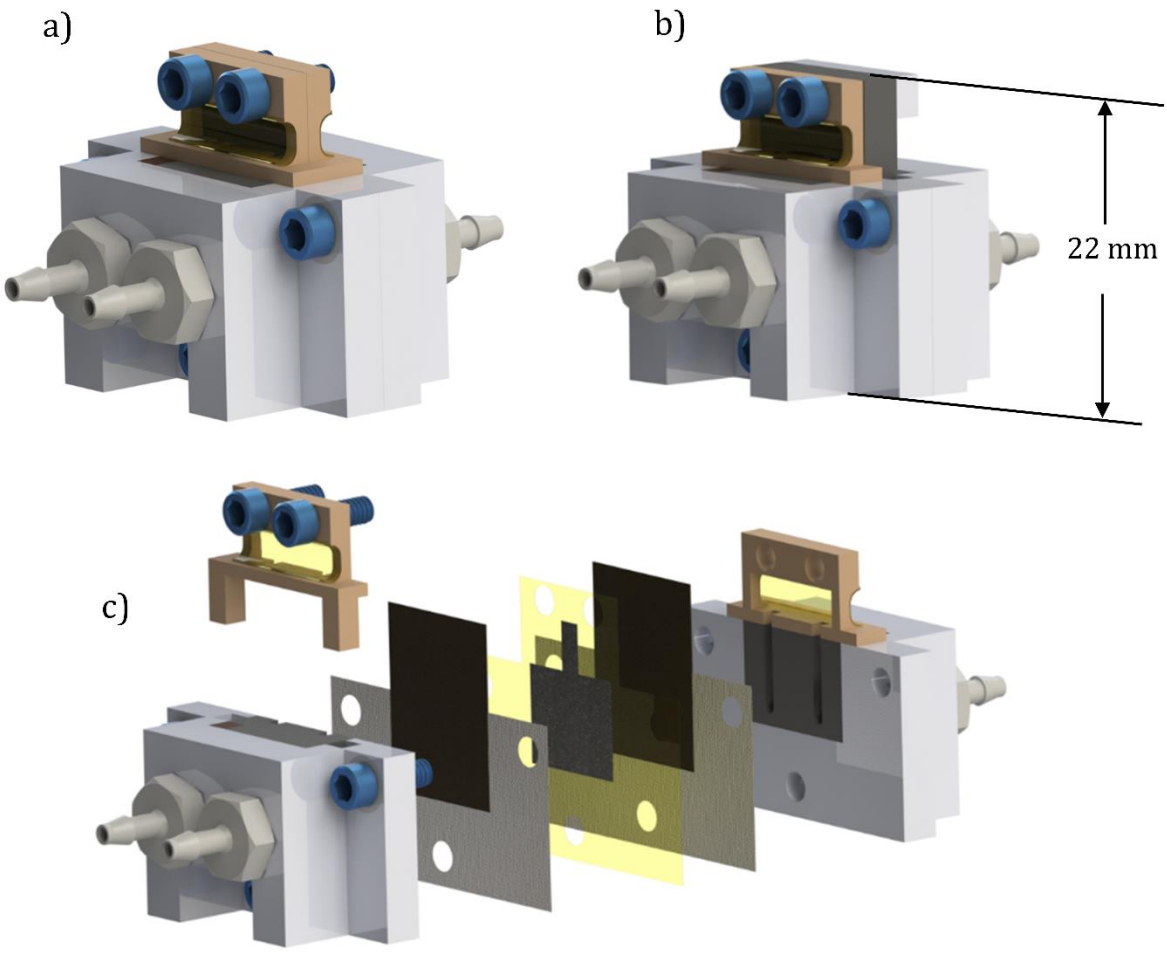

Figure 6-13. Generation IV nano CT cell a) flow chamber cell b) half-graphite cell c) exploded view of flow chamber cell

This cell will also be much cheaper to make, as the geometry is simpler and it does not require the extremely tight tolerances that the previous nano CT cell did.

6.7 *Chapter Conclusion*

Presented here is the development progression of a first of its kind hydrogen fuel cell for nano-scale x-ray CT study. Each successive generation of this cell has improved its electrochemical and imaging performance. The use of KB mirrors and high photon energy at the European Synchrotron produced by far the best results, so all future

operando experiments will be performed there. The generation IV cell presented here will offer a vast improvement over its predecessors in terms of electrochemical performance, versatility, and cost.

7 Conclusions and Future Work

7.1 *Conclusion*

This work presents several advances in the imaging of polymer electrolyte fuel cells. Of the techniques available, x-ray computed tomography (CT) is the best suited due to its ability to span micro and nano scales, its ability to image through sample holders, and its non-destructiveness. A rigorous derivation of the optical laws governing x-rays yielded a practical guide to experiment design. The most significant part of this derivation is the Beer-Lambert law, which—along with the complex attenuation coefficient—can aid in the selection of absorption vs phase contrast imaging. It can also aid in the design of *operando* sample holders as it can be used to predict the attenuation each component based on the material, its thickness, and the photon energy of the x-rays. The Beer-Lambert law also forms the basis of x-ray absorption near edge spectroscopy (XANES). XANES can be combined with many imaging techniques to find the location and concentration of elements in a solid by scanning above and below that element's x-ray absorption edge. XANES can also be used to separate features, a technique called two energy imaging.

Novel dispersed nanostructure thin film (dNSTF) electrodes are a promising alternative to conventional platinum/carbon catalysts due to their ability to combine the high activity of NSTFs with the durability of conventional electrodes. Understanding the morphology of these electrodes will speed up their development, as it will identify the strengths and

weaknesses of different designs. This work compared the mean radii of the platinum agglomerates for dNSTFs with two different carbon types using nano CT. The mean radius is a good measure of how effectively the Pt is being used as a small radius implies a high surface area to volume ratio, which is desired. The dNSTFs with high surface area carbon (HSAC) were found to have a lower mean Pt radius than those with medium surface area (MSAC) carbon for low Pt loadings, and equal Pt radii for high Pt loadings. The porous matrix of the dNSTFs was also studied, and the HSAC dNSTFs were also found to have higher porosity and lower tortuosity than the MSAC dNSTFs, indicating they will have less transport resistance.

Previous work studying ionomer distribution in catalyst layers used cesium staining to make the usually dim ionomer appear brightly in absorption contrast imaging. This posed a problem as there was no good way to differentiate between the platinum (Pt) and the cesium stained ionomer, as both have high attenuation coefficients. The solution presented here is to use two energy imaging. The first scan was taken below the Pt L3 absorption edge where Pt appears dimmer than Cs. The second scan was taken above the edge where Pt appears brighter than Cs. Using image subtraction, the Pt and Cs stained ionomer were definitely separated for the first time. This will greatly enhance the accuracy of the characterization of Pt/ionomer electrodes.

The pooling of water in the pores of fuel cell components, a condition known as flooding, is a significant problem for fuel cells. Due to the dynamic nature of the water production in the cell, this phenomenon must by studied with *operando* imaging. Previous attempts to visualize the water distribution in fuel cells used neutron imaging and micro CT. Neutron imaging lacks the resolution to see the structure of individual pores, so micro CT

is the optimal method. Presented here is the design of two novel fuel cells optimized for *operando* imaging. The first is a micro CT cell, which improved upon the previous state of the art cells in its electrical conductivity, mechanical compression, and ability to rapidly test multiple flow field designs. The second is a first of its kind nano CT cell, which offers the ability to see dynamic effects in nanometer resolution. This nanometer resolution is required for the visualization of the catalyst layer, which had previously never been imaged *in-operando*.

Platinum group metal (PGM)-free catalysts offer a distinct cost advantage over conventional Pt electrodes, due to the high cost of Pt. This study presents *operando* micro CT imaging of a Fe-N-C catalyst fuel cell for the first time. Due to the fact that Fe has a much lower activity than Pt, the catalyst layer is an order of magnitude thicker than conventional Pt catalysts. Due to the increased thickness, its morphology can be resolved using micro CT. Large voids were observed at the interface of the gas diffusion electrode (GDE) and the membrane. These voids were caused by the inhomogeneous evaporative drying of deposited ink on the GDL, as their size did not change when the compression level was varied. Water was observed to pool in these voids on the cathode side as well as in the cathode channel. This indicates that all of the water is being removed through the cathode channel as water was not observed on the anode side of the cell.

Radiography experiments with the nano CT cell revealed cracks forming in the catalyst coated membrane (CCM) with increased current density. First of their kind *operando* nanoscale full tomography experiments showed the catalyst layer of an *operando* cell on a continuum of resolutions from 323 nm to 50 nm.

7.2 *Future Work*

The two energy imaging technique presented in Chapter 4 should be applied to the dNSTF materials imaged in Chapter 3 in order to validate the results. This will greatly increase their reliability, as well as give valuable insight into the ionomer distribution in dNSTFs. The fourth generation nano CT cell presented here will provide significant improvements to the existing nano CT cell design. This cell should be imaged at the European Synchrotron (ESRF) due to the ability to easily vary both resolution and energy.

[1] J. Marie, R. Chenitz, M. Chatenet, S. Berthon-Fabry, N. Cornet, and P. Achard, "Highly porous PEM fuel cell cathodes based on low density carbon aerogels as Pt-support: Experimental study of the mass-transport losses," *Journal of Power Sources,* vol. 190, pp. 423-434, 2009.
[2] W. Epting, "Characterizing Electrode-Level Oxygen Transport in Polymer Electrolyte Fuel Cells," Doctor of Philosophy, Mechanical Engineering, Carnegie Mellon University, Pittsburgh, PA, 2015.
[3] G. T. Martinez, K. H. W. van den Bos, M. Alania, P. D. Nellist, and S. Van Aert, "Thickness dependence of scattering cross-sections in quantitative scanning transmission electron microscopy," *Ultramicroscopy,* vol. 187, pp. 84-92, Apr 2018.
[4] E. Coz, J. Théry, P. Boillat, V. Faucheux, D. Alincant, P. Capron, *et al.*, "Water management in a planar air-breathing fuel cell array using operando neutron imaging," *Journal of Power Sources,* vol. 331, pp. 535-543, 2016.
[5] J. Seweryn, J. Biesdorf, T. J. Schmidt, and P. Boillat, "Communication—Neutron Radiography of the Water/Gas Distribution in the Porous Layers of an Operating Electrolyser," *Journal of The Electrochemical Society,* vol. 163, pp. F3009-F3011, 2016.
[6] I. Manke, C. Hartnig, M. Grünerbel, W. Lehnert, N. Kardjilov, A. Haibel, *et al.*, "Investigation of water evolution and transport in fuel cells with high resolution synchrotron x-ray radiography," *Applied Physics Letters,* vol. 90, p. 174105, 2007.
[7] A. Schneider, C. Wieser, J. Roth, and L. Helfen, "Impact of synchrotron radiation on fuel cell operation in imaging experiments," *Journal of Power Sources,* vol. 195, pp. 6349-6355, 2010.
[8] J. Eller, T. Rosen, F. Marone, M. Stampanoni, A. Wokaun, and F. N. Büchi, "Progress in In Situ X-Ray Tomographic Microscopy of Liquid Water in Gas Diffusion Layers of PEFC," *Journal of The Electrochemical Society,* vol. 158, 2011.
[9] R. T. White, F. P. Orfino, M. E. Hannach, O. Luo, M. Dutta, A. P. Young, *et al.*, "3D Printed Flow Field and Fixture for Visualization of Water Distribution in Fuel Cells by X-ray Computed Tomography," *Journal of The Electrochemical Society,* vol. 163, pp. F1337-F1343, 2016.
[10] L. Grodzins, "Optimum Energies for X-Ray Transmission Tomography of Small Samples," *Nuclear Instruments and Methods,* vol. 206, pp. 541-545, 1982.
[11] C. Lim, H. Kang, V. De Andrade, F. De Carlo, and L. Zhu, "Hard X-ray-induced damage on carbon-binder matrix for in situ synchrotron transmission X-ray microscopy tomography of Li-ion batteries," *J Synchrotron Radiat,* vol. 24, pp. 695-698, May 1 2017.
[12] S. A. Vaselabadi, D. Shakarisaz, P. Ruchhoeft, J. Strzalka, and G. E. Stein, "Radiation damage in polymer films from grazing-incidence X-ray scattering

measurements," *Journal of Polymer Science Part B: Polymer Physics,* vol. 54, pp. 1074-1086, 2016.
[13] J. Eller, J. Roth, F. Marone, M. Stampanoni, A. Wokaun, and F. N. Büchi, "Implications of polymer electrolyte fuel cell exposure to synchrotron radiation on gas diffusion layer water distribution," *Journal of Power Sources,* vol. 245, pp. 796-800, 1/1/ 2014.
[14] A. D. Shum, D. Y. Parkinson, X. Xiao, A. Z. Weber, O. S. Burheim, and I. V. Zenyuk, "Investigating Phase-Change-Induced Flow in Gas Diffusion Layers in Fuel Cells with X-ray Computed Tomography," *Electrochimica Acta,* vol. 256, pp. 279-290, 2017.
[15] D. P. Finegan, M. Scheel, J. B. Robinson, B. Tjaden, I. Hunt, T. J. Mason, *et al.*, "In-operando high-speed tomography of lithium-ion batteries during thermal runaway," *Nat Commun,* vol. 6, p. 6924, Apr 28 2015.
[16] H. Xu, M. Bührer, F. Marone, T. J. Schmidt, F. N. Büchi, and J. Eller, "Fighting the Noise: Towards the Limits of Subsecond X-ray Tomographic Microscopy of PEFC," *ECS Transactions,* vol. 80, pp. 395-402, 2017.
[17] N. Srisutthiyakorn and G. M. Mavko, "What is the role of tortuosity in the Kozeny-Carman equation?," *Interpretation,* vol. 5, pp. SB57-SB67, 2017.
[18] N. Epstein, "On tortuosity and the tortuosity factor in flow and diffusion through porous media," *Chemical Engineering Science,* vol. 44, pp. 779-781, 1988.
[19] P. C. Carman, *Flow of Gases Through Porous Media*. London: Butterworths Scientific Publications, 1956.
[20] B. Tjaden, D. P. Finegan, J. Lane, D. J. L. Brett, and P. R. Shearing, "Contradictory concepts in tortuosity determination in porous media in electrochemical devices," *Chemical Engineering Science,* vol. 166, pp. 235-245, 2017.
[21] B. Tjaden, J. Lane, P. J. Withers, R. S. Bradley, D. J. L. Brett, and P. R. Shearing, "The application of 3D imaging techniques, simulation and diffusion experiments to explore transport properties in porous oxygen transport membrane support materials," *Solid State Ionics,* vol. 288, pp. 315-321, 2016.
[22] M. Barrande, R. Bouchet, and R. Denoyel, "Tortuosity of porous particles," *Anal Chem,* vol. 79, pp. 9115-21, Dec 01 2007.
[23] T. A. Watson and C. T. P. Chang, "Characterizing porous media with NMR methods," *Progress in Nuclear Magnetic Resonance Spectroscopy,* 1997.
[24] S. J. Cooper, A. Bertei, P. R. Shearing, J. A. Kilner, and N. P. Brandon, "TauFactor: An open-source application for calculating tortuosity factors from tomographic data," *SoftwareX,* vol. 5, pp. 203-210, // 2016.
[25] M. Fox, *Optical Properties of Solids*. Oxford, UK: Oxford UP, 2001.
[26] M. Born and E. Wolf, *Principles of Optics*, 7 ed. Cambridge, UK: Cambridge UP, 1959.
[27] A. Thompson, D. Attwood, E. Gullikson, M. Howells, K. Kim, J. Kirz, *et al.*, "X-Ray Data Booklet," L. B. N. Laboratory, Ed., 3 ed. Berkeley, CA, 2009.
[28] J. Als-Nielsen and D. McMorrow, "Imaging," in *Elements of Modern X-ray Physics*, 2 ed. Hoboken, NJ: John Wiley & Sons, Inc., 2011.

[29] C. T. Chantler, K. Olsen, R. A. Dragoset, J. Chang, S. A. Kotochigova, and D. S. Zucker, "X-Ray Form Factor, Attenuation, and Scattering Tables ", N. P. M. Laboratory, Ed., ed, 2001.
[30] A. Tkachuk, F. Duewer, H. Cui, M. Feser, S. Wang, and W. Yun, "X-ray computed tomography in Zernike phase contrast mode at 8 keV with 50-nm resolution using Cu rotating anode X-ray source," *Zeitschrift für Kristallographie - Crystalline Materials*, vol. 222, 2007.
[31] Z. Yin, T. Kanade, and M. Chen, "Understanding the phase contrast optics to restore artifact-free microscopy images for segmentation," *Med Image Anal*, vol. 16, pp. 1047-62, Jul 2012.
[32] J. N. Weker and M. F. Toney, "Emerging In Situ and Operando Nanoscale X-Ray Imaging Techniques for Energy Storage Materials," *Advanced Functional Materials*, vol. 25, pp. 1622-1637, 2015.
[33] J. Simmons and K. Potter, *Optical Materials*. San Diego, CA: Academic Press, 2000.
[34] A. Kongkanand and M. F. Mathias, "The Priority and Challenge of High-Power Performance of Low-Platinum Proton-Exchange Membrane Fuel Cells," *The Journal of Physical Chemistry Letters*, vol. 7, pp. 1127-1137, 2016/04/07 2016.
[35] M. Lopez-Haro, L. Guetaz, T. Printemps, A. Morin, S. Escribano, P. H. Jouneau, *et al.*, "Three-dimensional analysis of Nafion layers in fuel cell electrodes," *Nat Commun*, vol. 5, p. 5229, Oct 30 2014.
[36] M. K. Debe, "Electrocatalyst approaches and challenges for automotive fuel cells," *Nature*, vol. 486, pp. 43-51, Jun 6 2012.
[37] M. K. Debe, A. J. Steinbach, and K. Noda, "Stop-Start and High-Current Durability Testing of Nanostructured Thin Film Catalysts for PEM Fuel Cells," *ECS Transactions*, vol. 3, pp. 835-853, October 20, 2006 2006.
[38] A. J. Steinbach, M. K. Debe, and A. T. Haug, "Fuel cell water management via reduced anode reactant pressure," ed: US Patent 9,276,273, 2016.
[39] A. J. Steinbach, M. K. Debe, J. Wong, M. J. Kurkowski, A. T. Haug, D. M. Peppin, *et al.*, "A New Paradigm for PEMFC Ultra-Thin Electrode Water Management at Low Temperatures," *ECS Transactions*, vol. 33, pp. 1179-1188, October 1, 2010 2010.
[40] S. Komini Babu, H. T. Chung, P. Zelenay, and S. Litster, "Resolving Electrode Morphology's Impact on Platinum Group Metal-Free Cathode Performance Using Nano-CT of 3D Hierarchical Pore and Ionomer Distribution," *ACS Appl Mater Interfaces*, vol. 8, pp. 32764-32777, Dec 7 2016.
[41] S. J. Lee, S. Mukerjee, J. McBreen, Y. W. Rho, Y. T. Kho, and T. H. Lee, "Effects of Nafion impregnation on performances of PEMFC electrodes," *Electrochemica Acta*, vol. 43, pp. 3693-3701, 1998.
[42] F. C. Cetinbas, X. Wang, R. K. Ahluwalia, N. N. Kariuki, R. P. Winarski, Z. Yang, *et al.*, "Microstructural Analysis and Transport Resistances of Low-Platinum-Loaded PEFC Electrodes," *Journal of The Electrochemical Society*, vol. 164, pp. F1596-F1607, 2017.
[43] D. Gursoy, F. De Carlo, X. Xiao, and C. Jacobsen, "TomoPy: a framework for the analysis of synchrotron tomographic data," *J Synchrotron Radiat*, vol. 21, pp. 1188-93, Sep 2014.

[44] N. Otsu, "A Threshold Selection Method for Gray-Level Histograms," *IEEE*, 1979.
[45] C. Sha, J. Hou, and H. Cui, "A robust 2D Otsu's thresholding method in image segmentation," *Journal of Visual Communication and Image Representation*, vol. 41, pp. 339-351, 2016.
[46] M. Doube, M. M. Klosowski, I. Arganda-Carreras, F. P. Cordelieres, R. P. Dougherty, J. S. Jackson, *et al.*, "BoneJ: Free and extensible bone image analysis in ImageJ," *Bone*, vol. 47, pp. 1076-9, Dec 2010.
[47] J. Schindelin, I. Arganda-Carreras, E. Frise, V. Kaynig, M. Longair, T. Pietzsch, *et al.*, "Fiji: an open-source platform for biological-image analysis," *Nat Methods*, vol. 9, pp. 676-82, Jun 28 2012.
[48] S. Rieberer and K. Norian, "Analytical electron microscopy of Nafion ion exchange membranes," *Ultramicroscopy*, 1992.
[49] Y. Liu, F. Meirer, P. A. Williams, J. Wang, J. C. Andrews, and P. Pianetta, "TXM-Wizard: a program for advanced data collection and evaluation in full-field transmission X-ray microscopy," *Journal of Synchrotron Radiation*, vol. 19, pp. 281-287, 2012.
[50] B. Bhattacharyya, "Electrochemical Machining," pp. 25-52, 2015.
[51] Simon, Hasché, Müller, and H. A. Gasteiger, "Influence of the Gas Diffusion Layer Compression on the Oxygen Mass Transport in PEM Fuel Cells," *ECS Transactions*, 2015 2015.
[52] R. G. Budynas and J. K. Nisbett, *Shigley's Mechanical Engineering Design*. New York, NY: McGraw-Hill, 2011.
[53] J. Millichamp, T. J. Mason, T. P. Neville, N. Rajalakshmi, R. Jervis, P. R. Shearing, *et al.*, "Mechanisms and effects of mechanical compression and dimensional change in polymer electrolyte fuel cells – A review," *Journal of Power Sources*, vol. 284, pp. 305-320, 2015.
[54] S. Toghyani, E. Afshari, E. Baniasadi, and S. A. Atyabi, "Thermal and electrochemical analysis of different flow field patterns in a PEM electrolyzer," *Electrochimica Acta*, vol. 267, pp. 234-245, 2018.
[55] M. D. Capelato, "An Easy and Practical Way To Solder Copper Wires on Graphite " *Journal of Chemical Education*, vol. 70, p. 431, 1993.
[56] I. V. Zenyuk, R. Taspinar, A. R. Kalidindi, E. C. Kumbur, and S. Litster, "Computational and Experimental Analysis of Water Transport at Component Interfaces in Polymer Electrolyte Fuel Cells," *Journal of the Electrochemical Society*, vol. 161, pp. F3091-F3103, 2014.
[57] T. Bergman, A. Lavine, F. Incropera, and D. Dewitt, *Fundamentals of Heat and Mass Transfer*, 7 ed.: Wiley.
[58] M. Ross. (2011). *K-B Mirrors Harness X-rays for Science* [Article].